AIAA JOURNAL
Vol. 45, No. 3, March 2007

Suppressing Aeroelastic Instability Using Broadband Passive Targeted Energy Transfers, Part 1:Theory

Young S. Lee,* Alexander F. Vakakis,† Lawrence A. Bergman,‡ D. Michael McFarland,§ and Gaëtan Kerschen¶
University of Illinois at Urbana–Champaign, Urbana, Illinois 61801

DOI: 10.2514/1.24062

We study passive and nonlinear targeted energy transfers induced by resonant interactions between a single-degree-of-freedom nonlinear energy sink (NES) and a 2-DOF in-flow rigid wing model. We show that it is feasible to partially or even completely suppress aeroelastic instability by passively transferring vibration energy from the wing to the NES in a one-way irreversible fashion. Moreover, this instability suppression is performed by partially or completely eliminating its triggering mechanism. Numerical parametric studies identify three main mechanisms for suppressing aeroelastic instability: recurring burstout and suppression, intermediate suppression, and complete elimination. We investigate these mechanisms both numerically by the Hilbert–Huang transform and analytically by a complexification-averaging technique. Each suppression mechanism involves strong 1:1 resonance capture during which the NES absorbs and dissipates a significant portion of energy fed from the flow to the wing. Failure of suppression is associated with restoring the underlying triggering mechanism of instability, which is a series of superharmonic resonance captures followed by escapes from resonance. Finally, using a numerical continuation technique, we perform a bifurcation analysis to examine sensitive dependence on initial conditions and thus robustness of instability suppression.

Nomenclature

b	=	semichord length, $c/2$, where c is a chord length
C	=	nondimensional coefficient for essentially nonlinear coupling stiffness, $b^2k_s/m\omega_\alpha^2$
$C_{L,\alpha}$	=	lift curve slope, $\partial C_L/\partial\alpha\|_{\alpha=0}$
c_1, c_2	=	nonlinear heave and pitch stiffness factors
d; δ	=	offset attachment of the NES to the wing, measured from and positive ahead of the elastic axis (e.a.); nondimensional offset, d/b
e; γ	=	location of the aerodynamic center (a.c.) measured from the e.a. (positive ahead of e.a.); its nondimensional parameter, e/b
h, α, z	=	heave (positive downward), pitch (positive clockwise), NES (positive downward) degrees of freedom
K_h, K_α	=	coefficients of linear heave and pitch stiffnesses
L, M	=	lift and aerodynamic moment acting at the a.c., respectively; the equivalent aerodynamic forces at the e.a. are $L_{\text{ea}} = L$ and $M_{\text{ea}} = M + eL \approx eL$ for small angles
m, I_α	=	mass of the airfoil and its mass moment of inertia with respect to the e.a.
m_s, k_s, c_s	=	mass, essentially nonlinear stiffness, and damping in the NES
q	=	dynamic pressure, $\frac{1}{2}\rho_\infty U^2$, where ρ_∞ is the density of the flow
r_α	=	radius of gyration of the cross section of the wing, $\sqrt{I_\alpha/(mb^2)}$
S	=	planform area of the wing
S_α; x_α	=	mass unbalance in the airfoil, mx_{cg}; its nondimensional parameter, $S_\alpha/(mb)$, x_{cg}/b
t, τ	=	physical and nondimensional times ($\tau = \omega_\alpha t$)
U	=	constant and uniform flow speed around the wing
x_{cg}	=	location of the center of gravity (c.g.) measured from the e.a. (positive aft of the e.a.)
y, v	=	nondimensional heave ($y = h/b$) and NES ($v = z/b$) modes
Δ^y, Δ^α	=	steady-state amplitude ratio in the heave and pitch modes
ϵ	=	mass ratio between the NES and the wing, m_s/m
Θ	=	reduced speed of the flow, $U/b\omega_\alpha$
λ	=	nondimensional linear viscous damping in the NES, $c_s/m_s\omega_\alpha$
μ	=	density ratio, $\rho_\infty bS/2m$
ξ_y, ξ_α	=	nondimensional nonlinear heave and pitch stiffness factors ($\xi_y = c_1b^2\Omega^2$, $\xi_\alpha = c_2r_\alpha^2$)
Ω	=	frequency ratio, ω_h/ω_α, where $\omega_h = \sqrt{K_h/m}$ and $\omega_\alpha = \sqrt{K_\alpha/I_\alpha}$

Subscripts

ac	=	aerodynamic center
ea	=	elastic axis
cg	=	center of gravity

Superscripts

$\cdot$	=	$\mathrm{d}/\mathrm{d}t$
$'$	=	$\mathrm{d}/\mathrm{d}\tau$

Received 23 March 2006; revision received 28 November 2006; accepted for publication 30 October 2006.

*Graduate Research Assistant; currently Visiting Assistant Professor, Department of Mechanical Science and Engineering.

†Adjunct Professor, Departments of Mechanical Science and Engineering and Aerospace Engineering; also Professor, School of Applied Mathematical and Physical Sciences, National Technical University of Athens, Athens, Greece.

‡Professor, Department of Aerospace Engineering. Associate Fellow AIAA.

§Research Associate Professor, Department of Aerospace Engineering. Senior Member AIAA.

¶Visiting Scholar, Department of Aerospace Engineering; currently Postdoctoral Researcher, Aerospace and Mechanical Engineering Department (LTAS), Université de Liège, Liège, Belgium.

I. Introduction

THE triggering mechanism of limit cycle oscillations (LCOs) of a wing due to aeroelastic instability was studied recently [1]. It

was numerically and analytically shown that a cascade of resonance captures (a phenomenon where a dynamical system comes to satisfy commensurable frequency relations over finite time durations, triggering vigorous energy exchanges between its subsystems) constitutes the LCO triggering mechanism: attraction to transient resonance captures (TRCs**), escapes from these captures, and finally, entrapments into permanent resonance captures (PRCs††). It was also concluded that an initial excitation by the flow of the heave mode acts as the triggering mechanism for the eventual activation of the pitch mode through nonlinear interactions involving the aforementioned resonance captures and escapes; the eventual excitation of the pitch mode signifies the appearance of an LCO of the wing in flow. It was noted that this type of sustained LCO is similar to vortex-induced resonant vibrations of a bluff body, where the fluid–structure interaction, yielding LCOs of the body immersed in the fluid flow, exhibits synchronization and lock-in between the vortex and vibration frequencies [2].

In general, efforts have been made to control LCOs by means of active control schemes [3,4] or autoparametric excitations [5,6]. Lee et al. [7] studied LCO suppression in the van der Pol (VDP) oscillator by means of passive and targeted energy transfers to either grounded or ungrounded configurations of nonlinear energy sinks (NESs); these were single-degree-of-freedom (SDOF) oscillators with essentially nonlinear (nonlinearizable, or nonlinear but possessing no linear term) stiffness and a linear viscous damper. When resonance captures between the primary (VDP) oscillator and the attachment occur, broadband vibration energy is transferred to the attachment in a one-way irreversible fashion, hence the label NES. Many fluid–structure interactions generating LCOs can be modeled by the VDP oscillator (e.g., the aforementioned bluff body immersed in flow). Therefore, Lee et al. demonstrated potential applicability of targeted energy transfers to eliminate and stabilize oscillatory instabilities of practical self-excited systems, such as aeroelastic flutter of a wing.

In this work we study suppression of aeroelastic instabilities (LCOs) in a 2-DOF rigid wing model with an attached NES. First, we perform computational parametric studies that clearly demonstrate (at least) three fundamental mechanisms of LCO suppression by means of targeted energy transfers. In Sec. III, we further investigate the LCO suppression mechanisms numerically by performing time–frequency analysis by means of wavelet and Hilbert–Huang transforms (HHTs); and also analytically by using a two-frequency complexification–averaging technique. By computing energy dissipation by the NES against the energy input fed from a flow, we explore the energetic transactions associated with each mechanism in terms of instantaneous energy exchanges between modes. Furthermore, it is shown that resonance captures occur dominantly between same frequency components of each mode, during which strong targeted energy transfers from the wing to the NES occur. Section IV deals with robustness problems of LCO suppression by means of steady-state bifurcation analysis, for which numerical continuation is implemented. In this study we also describe how the three suppression mechanisms are reflected in the bifurcation picture of the dynamics. Finally, experimental verification of these theoretical observations are presented in a companion paper [8].

II. Preliminary Numerical Study

We consider the concept of attaching an SDOF ungrounded NES to the 2-DOF rigid wing model [1] (Fig. 1), to study the efficacy of suppressing aeroelastic instabilities of the wing by means of passive targeted energy transfers to the attachment (NES). The main motivation for considering this configuration lies in our previous study of LCO triggering mechanisms in the wing with no NES attached; indeed, as shown in Lee et al. [1], an initial excitation of the heave mode of the wing acts as the triggering mechanism for the development of LCOs with the wing oscillating predominantly in its pitch mode. Moreover, both the initial excitation (trigger) of the heave mode and the eventual development of the LCO are transient phenomena, and they involve broadband energy exchanges between the flow and the wing, as well as between the heave and pitch modes. It follows that a successful strategy for aeroelastic instability suppression should address directly the transient problem and not the steady-state one (i.e., after the full LCO has developed).

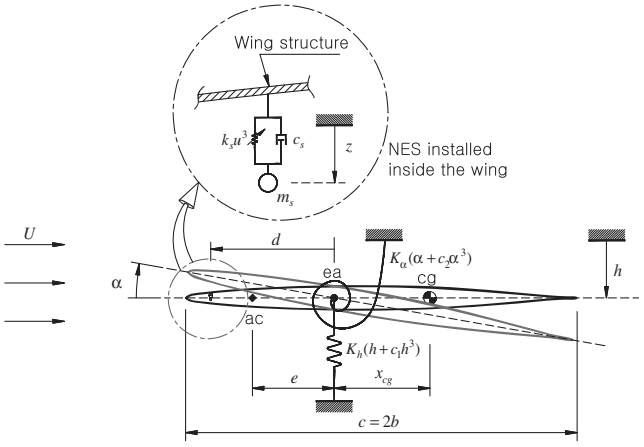

Fig. 1 Two-DOF rigid wing model coupled with an SDOF NES.

Consider the 2-DOF rigid wing model integrated with an SDOF NES in Fig. 1. Assuming small motions and using the principle of virtual work [9], we derive the equations of motion of the wing-NES assembly as

$$\begin{aligned}
&m\ddot{h} + S_\alpha\ddot{\alpha} + K_h(h + c_1h^3) + qSC_{L,\alpha}(\alpha + \dot{h}/U) \\
&\quad + c_s(\dot{h} - d\dot{\alpha} - \dot{z}) + k_s(h - d\alpha - z)^3 = 0 \\
&I_\alpha\ddot{\alpha} + S_\alpha\ddot{h} + K_\alpha(\alpha + c_2\alpha^3) - qeSC_{L,\alpha}(\alpha + \dot{h}/U) \\
&\quad + dc_s(d\dot{\alpha} + \dot{z} - \dot{h}) + dk_s(d\alpha + z - h)^3 = 0 \\
&m_s\ddot{z} + c_s(\dot{z} + d\dot{\alpha} - \dot{h}) + k_s(z + d\alpha - h)^3 = 0
\end{aligned} \tag{1}$$

or in nondimensional form,

$$\begin{aligned}
&y'' + x_\alpha\alpha'' + \Omega^2 y + \xi_y y^3 + \mu C_{L,\alpha}\Theta(y' + \Theta\alpha) + \epsilon\lambda(y' - \delta\alpha' \\
&\quad - v') + C(y - \delta\alpha - v)^3 = 0 \\
&r_\alpha^2\alpha'' + x_\alpha y'' + r_\alpha^2\alpha + \xi_\alpha\alpha^3 - \gamma\mu C_{L,\alpha}\Theta(y' + \Theta\alpha) + \delta\epsilon\lambda(\delta\alpha' \\
&\quad + v' - y') + \delta C(\delta\alpha + v - y)^3 = 0 \\
&\epsilon v'' + \epsilon\lambda(v' + \delta\alpha' - y') + C(v + \delta\alpha - y)^3 = 0
\end{aligned} \tag{2}$$

Note that the NES (z or v) interacts not only with the heave mode (h or y) but also with the pitch α through the offset d (or δ) from the elastic axis. We now perform computational parametric studies of the dynamics of (2) to identify parameter subsets where LCOs of the wing can be suppressed or even completely eliminated. Initial conditions close to the trivial equilibrium position are considered; that is, we set all initial conditions equal to zero except for the initial velocity $y'(0) = 0.01$. Regarding the wing parameters, we take these identical to the ones used in the earlier study by Lee et al. [1]:

$$\begin{aligned}
&x_\alpha = 0.2, \qquad r_\alpha = 0.5, \qquad \gamma = 0.4, \qquad \Omega = 0.5 \\
&\mu = (10\pi)^{-1}, \qquad C_{L,\alpha} = 2\pi, \qquad \xi_y = \xi_\alpha = 1
\end{aligned}$$

which gives a flutter speed $\Theta_F = 0.87$.

There are four control parameters for the NES: the mass ratio of the NES and the wing, ϵ; the damping coefficient λ; the coefficient of the essentially nonlinear stiffness C; and the offset attachment δ. In this study, we confine the parameter variations to the ranges $0.01 \le \epsilon \le 0.1$ (as small mass ratio as possible for reasons of practical implementation), $0.1 \le \lambda \le 1$, $1 \le C \le 20$, and $-1 \le \delta \le 1$.

**Resonance captures sustained for a certain period of time with subsequent escapes of the dynamics from the resonance manifolds

††Resonance captures sustained permanently

Our methodology for performing the computational parametric study is as follows: using the aforementioned initial conditions and parameter sets, we integrate the equations of motion (2) for sufficiently long time to assure that transients die out. Then we compute the rms amplitude of the resulting steady-state response. Comparing the steady-state pitch (or heave) amplitudes in rms with and without NES attached, we may infer partial or complete LCO suppression. Partial suppression of the LCO can be defined as the amplitude ratio (in the pitch mode) with and without NES attached, which should be less than 1; complete LCO suppression is inferred when this amplitude ratio tends to zero as the steady state of the system is reached. More specifically, we introduce the following definition for the amplitude ratio in the pitch mode:

$$\Delta^{\alpha} = \frac{\text{Steady-state pitch amplitude in rms with the NES}}{\text{Steady-state pitch amplitude in rms without the NES}} \times 100(\%) \tag{3}$$

and a similar expression for the heave mode (Δ^{y}).

Figure 2 depicts steady-state amplitude ratio in the pitch mode when the mass ratios are $\epsilon = 0.01$ and 0.02 for reduced speeds $\Theta = 0.9$ and 0.95, respectively. Here we only consider the reduction in the pitch mode because the pitch mode is generally dominant at the steady state, and the amplitude behavior of the NES is similar to that of the pitch mode. From these numerical computations, we first observe that LCO suppression is more probable when the NES is attached far from the elastic axis of the wing. The possible reason for this is that, for relatively large offsets, the NES interacts efficiently with both heave and pitch modes. Moreover, it seems that attaching the NES aft of the elastic axis (i.e., $\delta < 0$) provides more effective suppression. This can be inferred heuristically by examining Eq. (2); indeed, energy dissipation due to the damping term, $\epsilon\lambda(y' - \delta\alpha' - v')$, is maximized if the NES interacts with both heave and pitch modes under the influence of 1:1 resonance capture, and δ is negative. This will be revisited in the last section of this work. We also note that, if we want to retain suppression for increased flow speeds, we might need to consider higher mass ratios of the NES; for example, most of the regions where instability is suppressed by about 40% with $\epsilon = 0.01$ for $\Theta = 0.9$ (the area enclosed by thick curves in Fig. 2a) disappear when the same mass ratio is used for $\Theta = 0.95$ (Fig. 2c). Finally, we remark that this computational parametric study provides simple comparison of steady-state amplitude reductions (more precisely, average power reductions) under some specific initial conditions. A more detailed study should be related to the steady-state bifurcation structure of the dynamics of this system.

From the computational parametric study, we deduce the existence of three suppression mechanisms of LCOs, which are depicted in Figs. 3–5; Fig. 6 presents the case where the NES fails to suppress the aeroelastic instability. By studying the preliminary numerical results, some general conclusions are drawn regarding the dynamics of LCO suppression by the NES. It appears that the

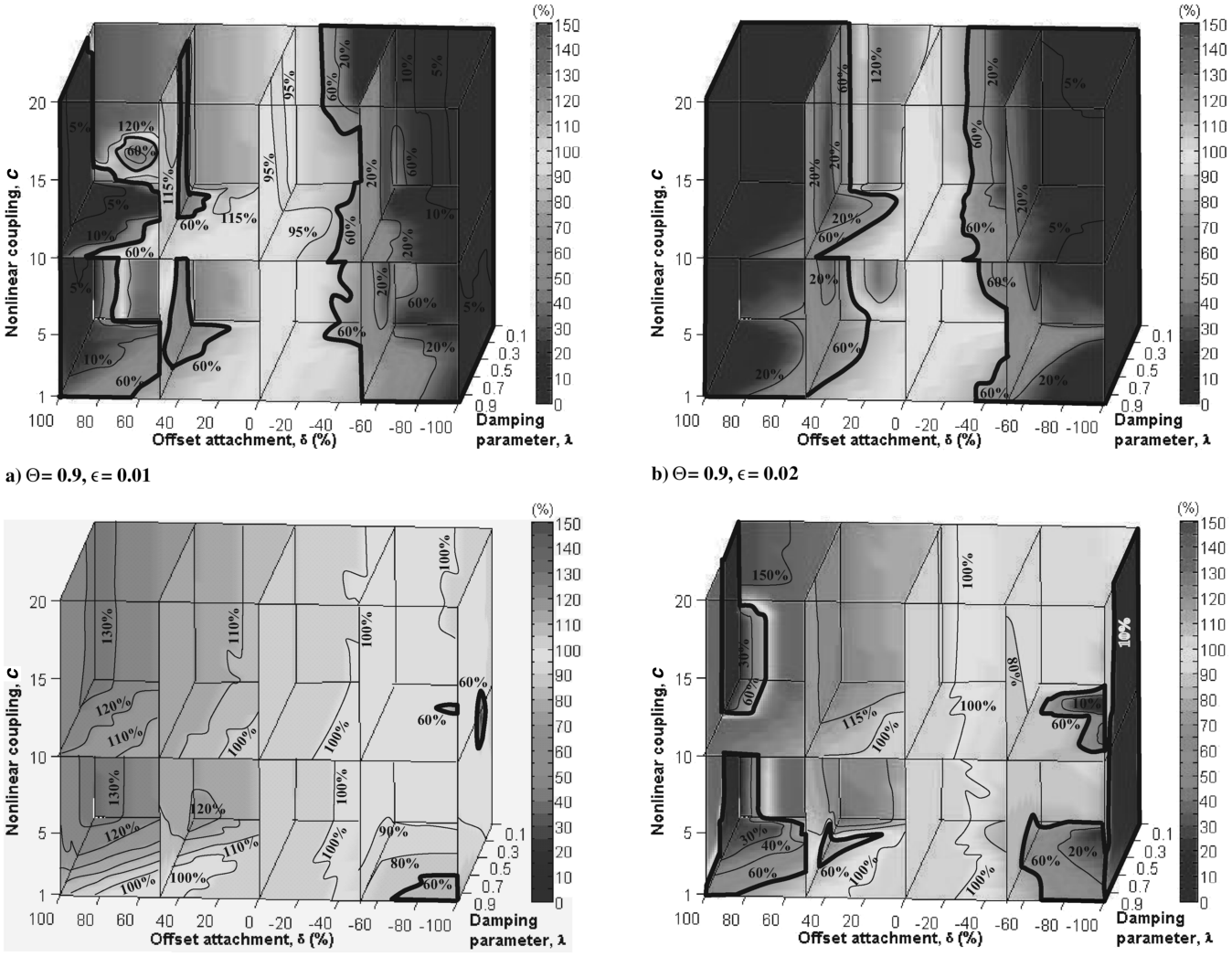

a) Θ= 0.9, ϵ= 0.01

b) Θ= 0.9, ϵ= 0.02

c) Θ= 0.95, ϵ= 0.01

d) Θ= 0.95, ϵ= 0.02

Fig. 2 Steady-state amplitude ratio in the pitch mode, Δ^{α}: The areas enclosed by the thick curves indicate the parameter domain where the amplitude ratio is less than 60%; the steady-state pitch amplitudes in rms without applying the NES are 0.11 rad for $\Theta = 0.9$ and 0.17 rad for $\Theta = 0.95$, respectively; initial conditions are all zero except $y'(0) = 0.01$.

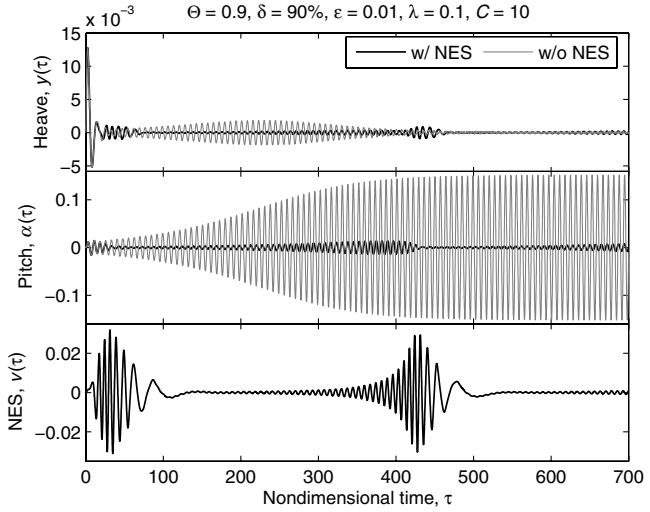

Fig. 3 The first suppression mechanism when $\Theta = 0.9$, $\delta = 90\%$, $\epsilon = 1\%$, $\lambda = 0.1$, and $C = 10$. All zero initial conditions except $y'(0) = 0.01$ are used.

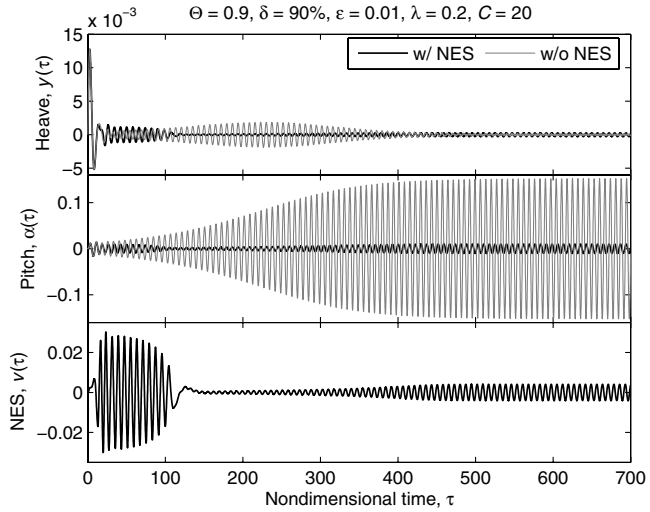

Fig. 4 The second suppression mechanism when $\Theta = 0.9$, $\delta = 90\%$, $\epsilon = 1\%$, $\lambda = 0.2$, and $C = 20$. All zero initial conditions except $y'(0) = 0.01$ are used.

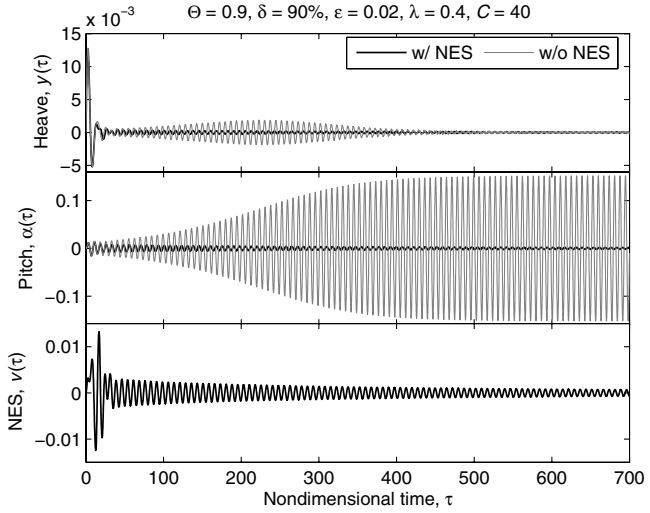

Fig. 5 The third suppression mechanism when $\Theta = 0.9$, $\delta = 90\%$, $\epsilon = 1\%$, $\lambda = 0.4$, and $C = 40$. All zero initial conditions except $y'(0) = 0.01$ are used.

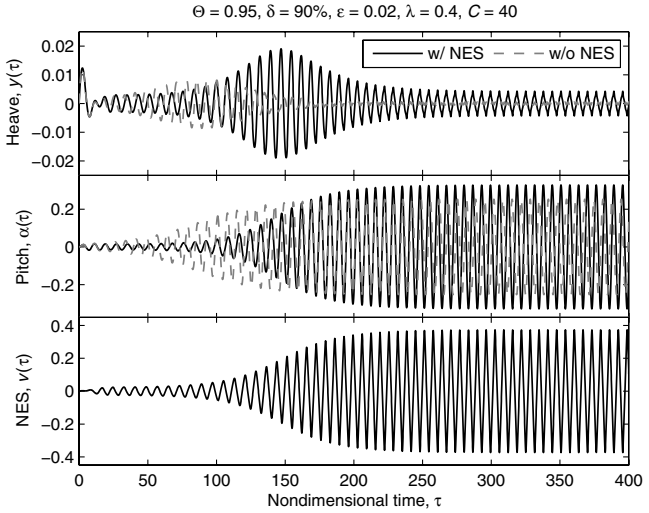

Fig. 6 No suppression when $\Theta = 0.95$, $\delta = 90\%$, $\epsilon = 2\%$, $\lambda = 0.4$, and $C = 40$. All zero initial conditions except $y'(0) = 0.01$ are used.

essential nonlinearity in the NES initially prevents the LCOs from growing above a certain amplitude; at a later phase of the response, conditions for resonance capture between the wing and the NES are fulfilled and passive targeted energy transfers from the wing to the NES take place leading to further LCO suppression.

We now provide a synoptic presentation of the three basic LCO suppression mechanisms identified in the numerical simulations, focusing only on their main dynamical features and leaving further details to the next section.

A. First Suppression Mechanism (Fig. 3)

This mechanism is characterized by a recurrent series of suppressed burstouts of the heave and pitch modes of the wing, followed by eventual complete suppression of the aeroelastic instabilities. In the initial phase of transient burstouts, a series of developing instabilities of predominantly the heave mode is effectively suppressed by proper transient "activation" of the NES, which tunes itself[‡‡] to the fast frequency of the developing aeroelastic instability; as a result, the NES engages in 1:1 TRC with the heave mode, passively absorbing broadband energy from the wing, thus eliminating the burstout. In the latter phase of the dynamics, the energy fed by the flow does not appear to directly excite the heave and pitch modes of the wing, but, instead, seems to get transferred directly to the NES until the wing is entirely at rest and complete LCO suppression is achieved. At the initial stage of the recurrent burstouts, at time instants when the pitching LCO is nearly eliminated, most of the energy induced by the flow to the wing is absorbed directly by the NES with only a small amount being transferred to the heave mode, so that both the NES and the heave mode reach their maximum amplitude modulations; this is followed by suppression of the burstout, and this process is repeated until at a later stage complete suppression of the aeroelastic instability is reached. The beatinglike (quasi-periodic) modal interactions observed during the recurrent burstouts turn out to be associated with Neimark–Sacker (NS) bifurcations [11] of a periodic solution and to be critical for determining domains of robust suppression.

B. Second Suppression Mechanism (Fig. 4)

This mechanism is characterized by intermediate or partial suppression of LCOs. The initial action of the NES is the same as in the first suppression mechanism. Targeted energy transfer to the NES

[‡‡]Because an NES possesses no preferential resonance frequency (i.e., due to the essential nonlinearity), the NES can interact in resonance with any mode of the primary system. By dissipating the transferred energy in its viscous damper, it can exhibit an escape from one resonance condition to another (theoretically, all the modes of the primary system), which is called self-detuning function of the NES [10].

then follows under conditions of 1:1 TRC, followed by conditions of 1:1 PRC, where both heave and pitch modes attain constant (but nonzero) steady-state amplitudes. We note that the heave mode response can grow larger than that in the corresponding system with no NES attached (exhibiting an LCO), at the expense of suppressing the pitch mode. We also note that, in contrast to the first suppression mechanism, the action of the NES is nonrecurring in this case, as it acts at the early phase of the motion stabilizing the wing and suppressing the LCO.

C. Third Suppression Mechanism (Fig. 5)

In this mechanism energy transfers from the wing to the NES are caused by nonlinear modal interactions during 1:1 resonance captures (RCs). Both heave and pitch modes as well as the NES exhibit exponentially decaying responses resulting in complete elimination of LCOs. In general, higher NES masses are required for complete elimination of LCOs for increasing reduced speeds.

D. No Suppression (Fig. 6)

This happens when the NES does not act as an efficient absorber of the energy input extracted from a fluid due to aeroelastic interaction. In some cases, as shown in the Fig. 6, the steady-state amplitudes of LCOs grow even larger than those of the corresponding system with no NES attached. Depending on the parameter values, the steady state may possess a superharmonic frequency relation between modes. Similar to the behavior observed in the LCO triggering mechanism in Lee et al. [1], in the case of no suppression there exists a transition from 1:1 to 3:1 locking of frequency ratios between the heave and pitch modes; this implies the occurrence of a 1:1 TRC followed by a transition to a 3:1 steady-state PRC between the heave and pitch modes. This observation suggests that, to suppress the aeroelastic instabilities, the NES must interact with both heave and pitch modes in such a way as to prevent direct energy transfer from the flow to the wing modes through subharmonic and superharmonic resonance captures (similar conclusions were drawn in Lee et al. [7], where LCO suppressions of a van der Pol oscillator were studied).

III. LCO Suppression Mechanisms

In this section, we investigate numerically and analytically the three LCO suppression mechanisms discussed in the preceding section. First, we will numerically postprocess the transient responses of the wing-NES assembly to determine the dominant harmonic components and the underlying nonlinear resonant interactions that produce targeted energy transfers and result in instability suppression in this system. The postprocessing techniques that will be employed include wavelet transforms (WTs) and empirical mode decompositions (EMDs) combined with Hilbert transforms (also called Hilbert–Huang transforms, or HHTs). Based on the numerical postprocessing results, we will analytically study the wing-NES dynamics by performing fast/slow partition of the transient dynamics using a multifrequency complexification–averaging technique; the resulting reduced-order slow-flow model will fully capture the wing-NES nonlinear interactions, and so can be used to fully understand and model the instability suppression mechanisms. This plan of study will provide a guideline for NES design to achieve effective LCO elimination.

A. Numerical Study

We first explore the nonlinear dynamics and energetic interactions governing each suppression mechanism in terms of instantaneous energy exchanges between modes. Because the system is self-excited, we compute the energetic exchanges related to each suppression mechanism numerically. The instantaneous total energy of the wing-NES assembly can be expressed as a sum of the instantaneous kinetic and potential energies of the wing and the NES:

$$E^{\text{Total}}(\tau) = \left[\frac{1}{2}y'(\tau)^2 + \frac{1}{2}r_\alpha^2\alpha'(\tau)^2 + x_\alpha y'(\tau)\alpha'(\tau) + \frac{1}{2}\epsilon v'(\tau)^2\right]_{\text{Kinetic}} + \left[\frac{1}{2}\Omega^2 y(\tau)^2 + \frac{1}{2}r_\alpha^2\alpha(\tau)^2 + \frac{1}{4}\xi_y y(\tau)^4 + \frac{1}{4}\xi_\alpha\alpha(\tau)^4\right]_{\text{Potential 1}} + \left[\frac{1}{4}C[y(\tau) - \delta\alpha(\tau) - v(\tau)]^4\right]_{\text{Potential 2}} \tag{4}$$

The energy dissipated by the viscous damper of the NES is given by

$$E_d^{\text{NES}}(\tau) = \epsilon\lambda\int_0^\tau \{v'(s) + \delta\alpha'(s) - y'(s)\}^2\,\mathrm{d}s \tag{5}$$

The input energy is a sum of the initial energy provided by the initial conditions and the nonconservative work done by the flow:

$$E^{\text{Input}}(\tau) = E^{\text{Total}}(0) + W_{nc}^{y}(\tau) + W_{nc}^{\alpha}(\tau) \tag{6}$$

where

$$W_{\text{nc}}^{y}(\tau) = \mu C_{L,\alpha}\Theta\int_0^\tau \{y'(s) + \Theta\alpha(s)\}y'(s)\,\mathrm{d}s$$

$$W_{\text{nc}}^{\alpha}(\tau) = -\gamma\mu C_{L,\alpha}\Theta\int_0^\tau \{y'(s) + \Theta\alpha(s)\}\alpha'(s)\,\mathrm{d}s$$

As a result, the instantaneous energy balance should hold:

$$E^{\text{Total}}(\tau) = E^{\text{Input}}(\tau) - E_d^{\text{NES}}(\tau) \tag{7}$$

Figure 7 depicts the instantaneous energy exchanges between modes (upper part), and the relation between energy input fed from a flow and energy dissipation by the NES (lower part), for each suppression mechanism. For comparison, the case where the LCO survives the action of the NES (case of no suppression) is also provided. Note that the depicted partition of the total energy into each wing mode assumes that the contribution to the potential energy of the essentially nonlinear coupling is assigned entirely to the NES part.

The study of the instantaneous modal energy exchanges indicates that the first suppression mechanism exhibits the most vivid energy interactions, especially between the pitch mode and the NES (Fig. 7a). The appearance of these modal interactions appears to be quite similar to the targeted energy transfer (TET) mechanisms studied in Kerschen et al. [10], and, in particular, TET initiated by nonlinear beat phenomena (resonance captures will be discussed later). In Sec. IV, we will explain this nonlinear beating behavior in terms of a study of steady-state bifurcations, whereby the first suppression mechanism is generated by the Neimark–Sacker bifurcation of a stable LCO (which is analogous to a Hopf bifurcation of an equilibrium) that generates another harmonic that yields quasi-periodic solutions in total. Hence, variation of the total energy shows repeated burstouts followed by suppressions with the energy input, E^{Input}, from the flow to the wing continuously increasing, nearly at the same rate with the energy dissipated by the NES, E_d^{NES}. At the time instant when a complete balance between E^{Input} and E_d^{NES} occurs, the total energy balance becomes zero; however, small disturbances from that totally balanced energetic state lead to recurring excitations of aeroelastic instabilities and the alternating series of suppressions and instability burstouts is continuously repeated. Note that, although the aeroelastic instabilities cannot be completely removed by this suppression mechanism, their amplitudes are greatly reduced compared to those developed when no NES is attached (Fig. 3).

The second suppression mechanism initially involves strong modal interactions so that a balance between energy input and dissipation is reached at the initial early stage of the motion (Fig. 7b). This vigorous initial energy exchange behavior resembles the fundamental TET mechanism (i.e., in-phase 1:1 resonance capture) discussed by Kerschen et al. [10]. Again, in this case, small disturbances can lead to reappearance of instabilities but with much

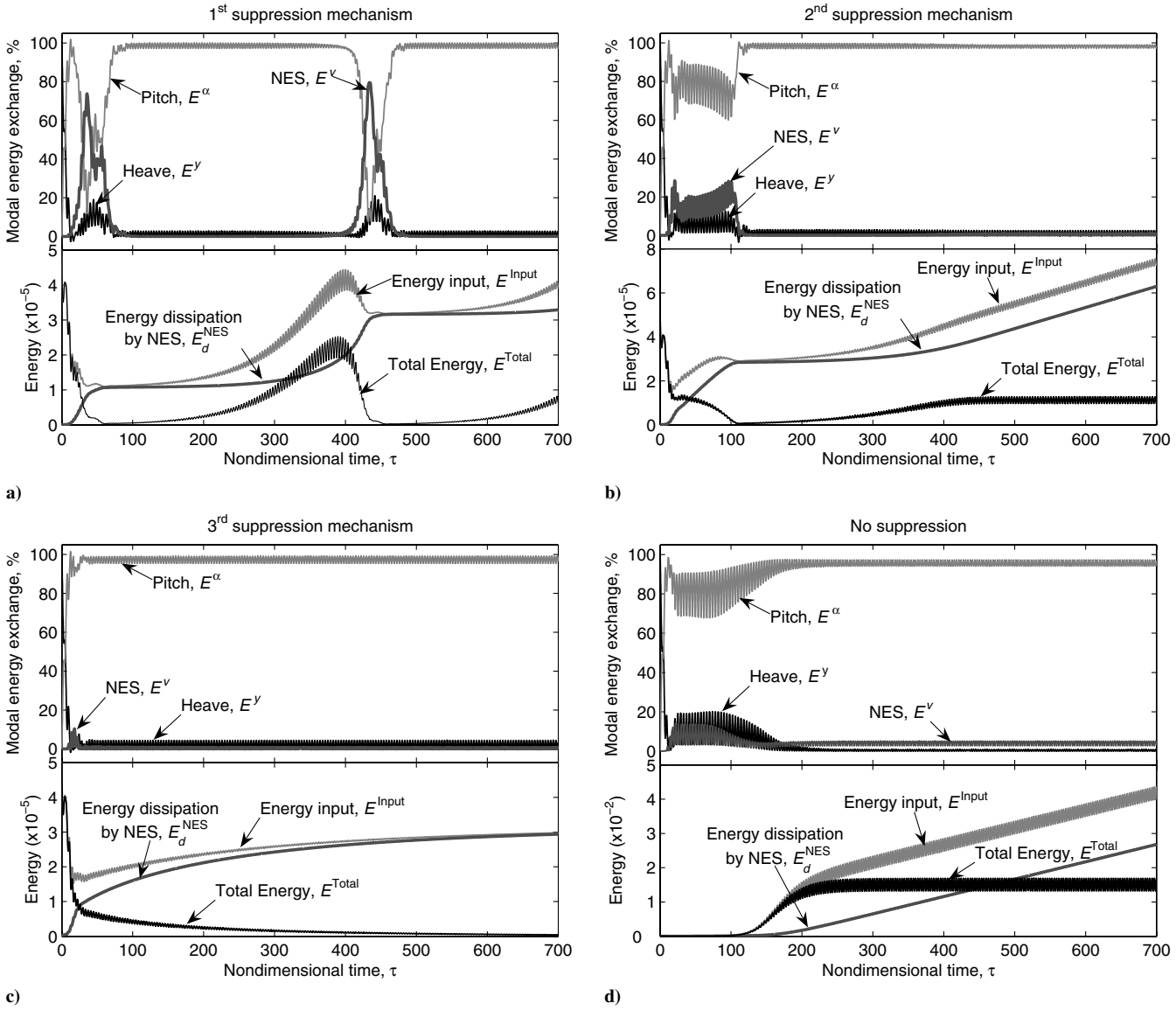

Fig. 7 Instantaneous energy exchanges between modes (upper), and comparison of input energy from flow and energy dissipation by the NES (lower). Parameters used in a)–d), respectively, correspond to those in Figs. 3–6.

smaller amplitudes (Fig. 4). The (increasing) rates of changes of energy input and energy dissipation by the NES become identical after a balance is reached (i.e., the averaged trends in the energy input and the dissipation follow parallel but noncoinciding paths), and their uniform difference makes possible the resulting reduced-amplitude LCOs. In a later section we will see that this mechanism is related to the generation of stable LCOs bifurcating from a stable trivial equilibrium after a supercritical Hopf bifurcation; however, the Hopf bifurcation point (i.e., the flutter speed), occurs above that of the corresponding system with no NES attached. The robustness of this suppression mechanism depends on the global bifurcation structure of the steady-state dynamics. This intermediate suppression will be destroyed under sufficiently large disturbances to yield LCOs with amplitudes greater than those realized in the wing with no NES attached. We will examine in detail this robustness of suppression in Sec. IV, by relating it to the steady-state bifurcation structure of the dynamics.

As for the third suppression mechanism (Fig. 7c), most of the total energy apparently remains confined in the pitch mode so that the wrong conclusion might be drawn that the NES does not work efficiently in this case. However, comparing the energy input and dissipation by the NES, we clearly observe that E_d^{NES} increases in the manner that energy balancing can occur only in the long run, thus preventing reappearance of LCOs in the long term. In other words, we can obtain complete elimination of LCOs in a robust way (depending on the global bifurcation structure of the dynamics, as will be discussed in Sec. IV).

Figure 7d shows the energy exchanges for a case where the LCO survives the action of the NES. Initially, there occur vigorous modal energy exchanges, but they occur predominantly between the heave and pitch modes, with only secondary involvement of the NES. This means that the action of the NES is not as effective as in the previous three suppression cases; as a result, the NES fails to prevent the energy interactions between the heave and pitch modes. Moreover, the energy dissipation by the NES is not sufficiently strong to make balance with the energy input fed from the flow, which "feeds" the modes of the wing, inducing aeroelastic instability. As a result, the LCOs are not only retained in this case, but their amplitudes become even larger than those realized in the wing with no NES attached (Fig. 6). Note that at steady state the NES continuously dissipates energy at a constant rate, which is nearly equal to the average rate of increase of the energy input from the flow. This behavior is similar to the second suppression mechanism except for the magnitude of the uniform distance between the two averaged parallel paths.

We now examine the time–frequency behavior of the transient responses by using the wavelet transform (WT). The WT involves a windowing technique with variable-sized regions so that it performs a multiresolution analysis, in contrast to the (fast) Fourier transform

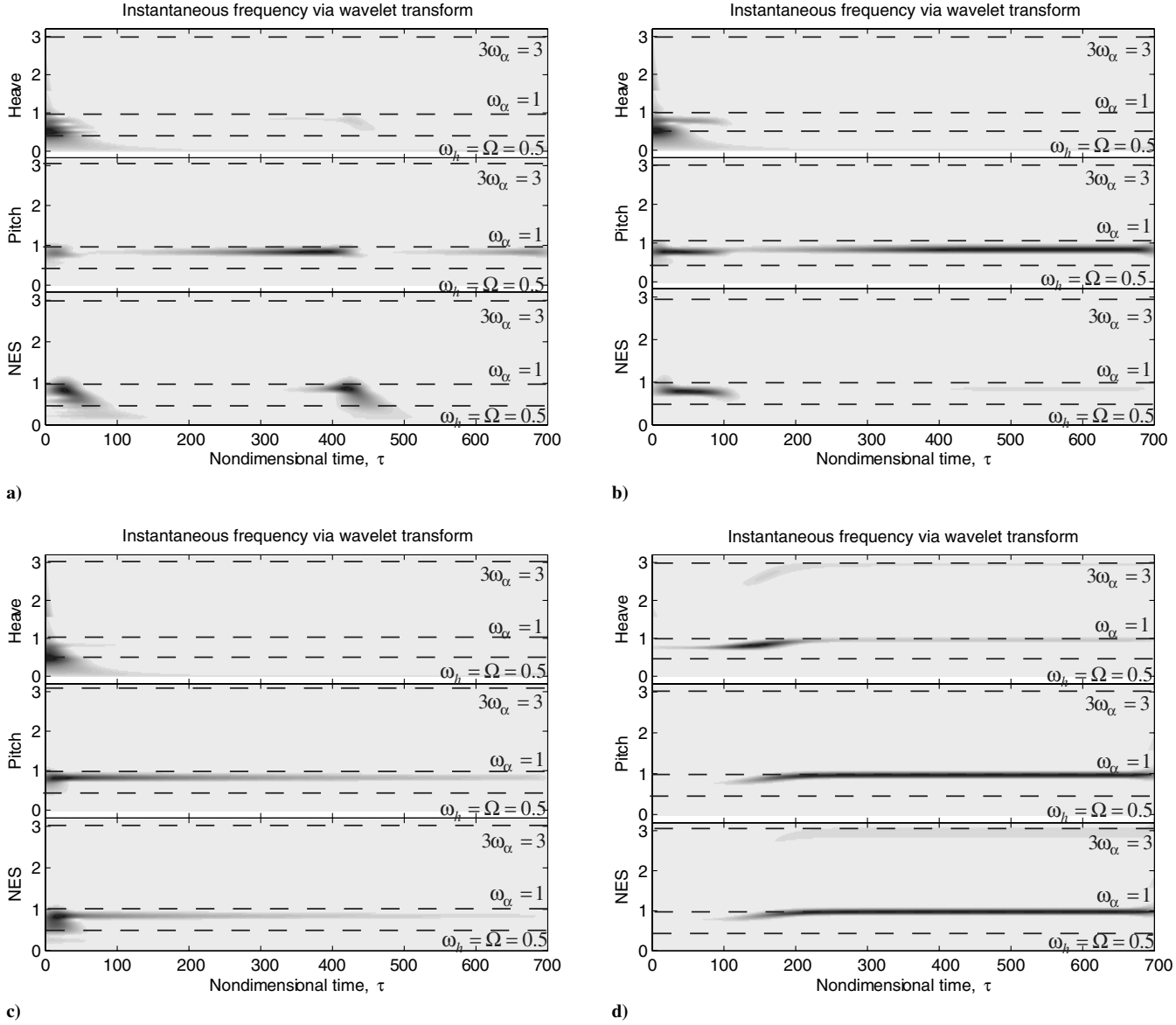

Fig. 8 Wavelet transforms showing time–frequency behavior of each suppression mechanism. Parameters used in a)–d), respectively, correspond to those in Figs. 3–6.

(FFT), which assumes signal stationarity. Small time intervals are considered for high-frequency components whereas the size of the interval is increased for lower-frequency components, thereby giving better time and frequency resolutions than the FFT. The Matlab® codes used for the WT computations in this work were developed at the Université de Liège (Liège, Belgium) by Dr. V. Lenaerts in collaboration with Dr. P. Argoul from the Ecole Nationale des Ponts et Chaussées (Paris, France). The Morlet wavelet, $\psi_M(\tau) = e^{-\tau^2/2} e^{j\omega_0 \tau}$, which is a Gaussian-windowed complex sinusoid of frequency ω_0, is considered as a mother wavelet in this study. The frequency ω_0 for the Morlet WT is a user-specified parameter that allows one to tune the frequency and time resolutions of the results.

Figure 8 presents the WT results applied to the responses in Figs. 3–6 (the three instability suppression mechanisms and the case of no suppression). The plots represent the amplitude of the WT as a function of frequency (vertical axis) and time (horizontal axis). Heavily shaded areas correspond to regions where the amplitude of the WT is high, whereas lightly shaded regions correspond to low amplitudes. Such plots enable one to deduce the temporal evolution of the dominant frequency components of the signals analyzed. Comparing the instantaneous frequency contents of the heave and pitch modes, and the NES, provides an additional (direct) way to verify the occurrence of resonance captures, or frequency locking in the transient dynamics.

First, we focus on the cases where partial or complete instability suppression occurs (Figs. 3–5). The results in Figs. 8a–8c indicate that primarily there occur 1:1 resonance interactions (captures) between the NES and the heave mode; in addition, there occur 1:1 resonance captures followed by transitions to subharmonic resonance captures between the NES and the pitch mode. Moreover, a common strong harmonic component in these results possesses a frequency near the natural frequency of the pitch mode (i.e., $\omega \approx 1$). Indirectly, these WTs suggest that in the study of all three suppression mechanisms one may use a two-frequency averaging method for analytically studying the previous suppression mechanisms (because at most two dominant frequency components appear in the transient responses governing the resonance interactions between various modes); that is, in all cases considered, the responses are dominated by two-frequency components with frequencies $\omega_h \approx \Omega = 0.5$ and $\omega_\alpha \approx 1$. This important finding will be implemented in the next section.

Focusing now on Figs. 6 and 8d, we make the additional remark that, when the LCO survives the action of the NES, the interaction between the heave and pitch modes completely resembles the behavior of the LCO triggering mechanism studied in Lee et al. [1];

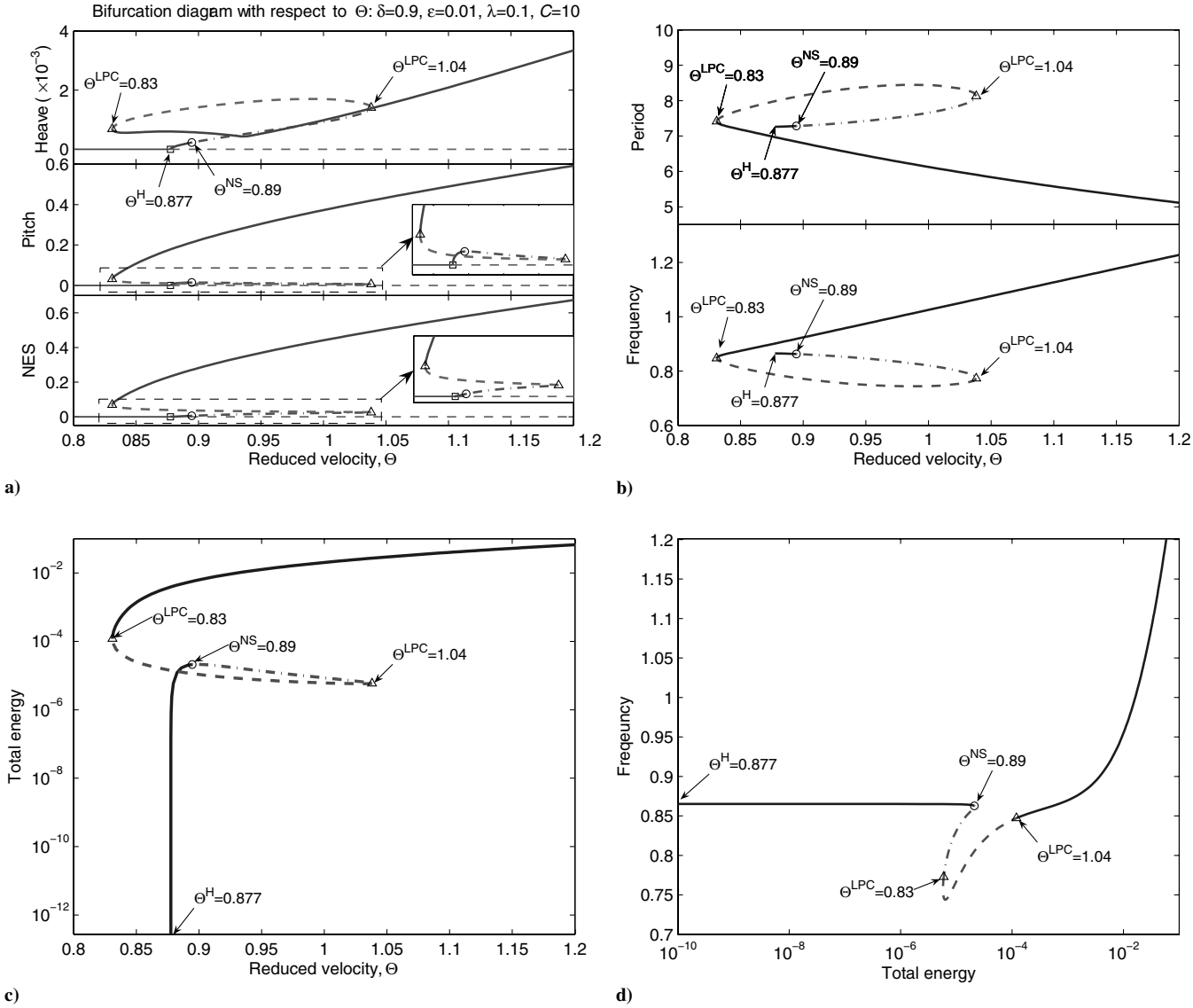

Fig. 9 Construction of a frequency–energy plot: a) bifurcation diagrams of the steady-state LCO amplitudes with respect to the reduced velocity, b) computed period and frequency, c) total energy as a function of Θ, and d) frequency–energy plot containing LCO solutions ($\delta = 0.9, \epsilon = 0.01, \lambda = 0.1, C = 10$); H, NS, and LPC denote Hopf, Neimark–Sacker, and limit point cycle bifurcations, respectively.

that is, there occurs a transition from 1:1 to 3:1 resonance captures. Moreover, in this case, the NES possesses a higher superharmonic component, so that its interaction with the pitch mode also undergoes a transition from 1:1 to 3:1 resonance captures. It follows that in this case the resonance interactions between the various modes of the wing-NES assembly are qualitatively different than those taking place in the three cases where LCO suppression is achieved.

Combining Figs. 7 and 8, we can construct the so-called frequency–energy plot (FEP), which is one of the useful tools to present dynamic transitions (i.e., 1:1, subharmonic, and superharmonic resonance captures, and escapes from resonances) between branches of periodic motions of an appropriately defined underlying Hamiltonian system (that is, a Hamiltonian system whose perturbation leads to the system of equations under consideration). The FEP for a single-DOF system coupled with a small mass through essentially nonlinear stiffness was computed to show that such a simple system may possess very complicated dynamics [12]; it was also implemented to examine basic mechanisms for the TETs [10]. The first application of the FEP to a self-excited system is found in Lee et al. [7], in which LCO elimination of a van der Pol oscillator using the NES was examined. It was shown that, when the LCO is completely eliminated, dynamic flow on the FEP follows a transition from a superharmonic to a 1:1 to a subharmonic resonance capture (the transitions between these subsequent resonance captures are characterized as "escapes from capture"). Elimination (and intermediate suppression as well) of LCO tends to prevent the dynamics from realizing transitions to superharmonic resonance captures between the NES and the primary system (in the case of Lee et al. [7], the VDP oscillator).

However, unlike the aforementioned studies [7,10,12], a definition of the FEP, which describes an underlying Hamiltonian structure of periodic solution, becomes difficult in the current problem. This is mainly due to the aeroelastic terms that provide nonconservative work to the system and change intrinsic natural frequencies with respect to the flow speed (and thus the total energy of the system). Hence, we propose another way of constructing the FEP for aeroelastic systems, based on the steady-state bifurcation structure that can be obtained numerically (e.g., using a numerical continuation technique) or analytically (e.g., multiphase averaging method or harmonic balance method). In this study, we implement a numerical continuation method by means of the code, MatCont [13], which will be used in Sec. IV.

Figure 9a depicts the bifurcation diagrams with respect to the reduced velocity Θ when the parameters used in Fig. 3 are considered. The stable LCOs born at Θ^H become unstable at Θ^{NS}, yielding new periodic components that amount to overall quasi-periodic motions on two tori. The branch of quasi-periodic motions is

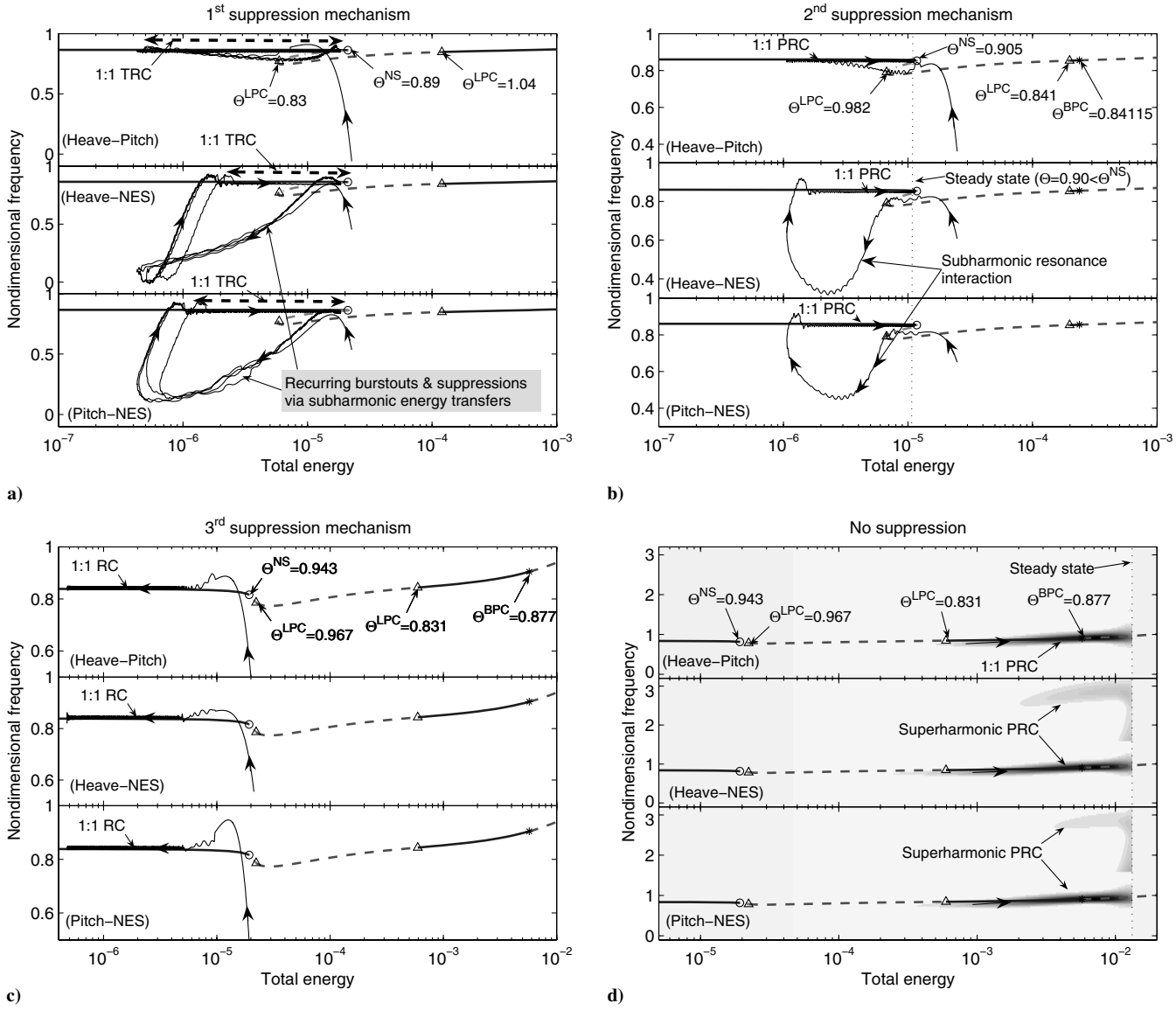

Fig. 10 LCO suppression mechanisms in the frequency–energy domain: the bold curves (solid for stability, dashed for instability, and dash-dotted for quasi-periodic instability) indicate intrinsic LCO branches obtained from the continuation method, which are analogous to the periodic solution branches of the underlying Hamiltonian system of coupled oscillators [12]. The thin solid curves (heavily shaded area) represent the transient responses when LCO suppression occurs (does not occur). Parameters used in a)–d), respectively, correspond to those in Figs. 3–6; H, NS, and LPC denote Hopf, Neimark–Sacker, and limit point cycle bifurcations, respectively.

closely associated with the first LCO suppression mechanism (detailed bifurcation characteristics will be introduced in Sec. IV). In addition, the period of the LCOs is obtained when performing the numerical continuation of limit cycles (shown in the upper row of Fig. 9b). Hence, the (circular) frequency of the LCOs can be computed as 2π divided by the corresponding period (depicted in the lower row of Fig. 9b). It is noted that this numerical method may not provide information regarding the existence of multiple frequencies, if any. On the other hand, we already practiced computing the total energy of the system. Figure 9c depicts the mean value of the total energy at each reduced speed (note that the instantaneous total energy is oscillating around this mean value due to the nonlinear modal interactions, i.e., RCs; cf. Figure 7). Finally, we combine the frequencies in the lower row of Fig. 9b and the total energies in Fig. 9c to obtain the FEP in Fig. 9d. In this case, the FEP is parameterized with respect to the reduced speed Θ, and each point on the curve in the FEP implies the LCO that the system (2) can possess for a specific reduced speed with the corresponding total energy (averaged) and dominant frequency.

Now we examine the three suppression mechanisms on the FEP (Fig. 10). To demonstrate the instantaneous frequencies of each modal response, the Hilbert transform is used for the three suppression mechanisms, and wavelet transforms, for the case when the LCOs survive the action of the NES. In computing the instantaneous frequencies, we applied the *Savitzky–Golay* polynomial smoothing filter to remove high-frequency noisy signals caused by numerical differentiation of the phase.

Nonlinear modal interactions between heave and pitch modes are realized mainly through 1:1 resonance captures whether or not LCO suppression results. The first suppression mechanism (Fig. 10a) is characterized by repeated loops (corresponding to the recurrent burstouts and suppressions) consisting of transitions from 1:1 to subharmonic resonance captures (suppression stage), and then reversals back to 1:1 TRCs (burstout stage). Reflecting the intrinsic LCO solutions, we find the following interesting behavior in the first suppression mechanism: once the dynamics exceeds the Neimark–Sacker bifurcation point $\Theta^{\mathrm{NS}} = 0.89$ (note that the flow speed currently considered is $\Theta = 0.9$), because the heave and pitch modes are in 1:1 TRC, the only choice for the dynamics is to follow the unstable LCO branches (which might contain either periodic or quasi-periodic motions). Hence, the dynamics can only be captured into loops that lead to transitions into subharmonic resonances.

These repetitions (bursting outs and consequent suppressions) characterize the first suppression mechanism.

When intermediate suppression of LCOs occurs, the dynamic flow on the FEP forms a single loop involving transitions from 1:1 to subharmonic resonance captures and reversals back to 1:1 PRC when steady-state dynamics is reached (Fig. 10b). Complete LCO elimination involves 1:1 resonance captures before the dynamics escapes from resonance, at which point the NES has completely exhausted the energy input from the flow (Fig. 10c). Finally, we can observe the dynamic transition from 1:1 to superharmonic resonance captures between the NES and the aeroelastic modes when the LCOs survive the action of the NES (Fig. 10d). Comparing Figs. 10c and 10d corresponding to the same underlying structure of LCOs (i.e., same parameters were used), we conclude that whether the LCOs are suppressed or not depends on the state of the dynamics of the system when resonance capture occurs. That is, in Fig. 10c where complete LCO suppression occurs, the dynamics is captured into the domain of attraction of the stable LCO branch at a lower energy regime; whereas, in Fig. 10d where no LCO suppression occurs, the dynamics is entrapped in the domain of attraction of the stable LCO branch formed at a higher energy regime, involving superharmonic PRCs between the NES and the aeroelastic modes, and thus invoking development of LCOs with large amplitudes.

In summary, we propose the representation of the transient dynamics of the system on the FEP to explain why the 1:1 resonance captures are represented by near straight lines in the vicinity of the natural frequency of the pitch mode ($\omega \approx 1$). In particular, the first suppression mechanism exhibits escapes near the NS bifurcation point that causes the stable LCOs to possess quasi-periodic instability, the second suppression mechanism reaches its steady state at the energy value of the corresponding reduced velocity (i.e., $\Theta = 0.9 < \Theta^{\mathrm{NS}} = 0.905$ in Fig. 10b), and the same parameter values (i.e., the same underlying bifurcation structure of the intrinsic LCOs) can yield different results (raising issues of robustness which will be addressed in a later section), depending on the given energy value (i. e., the reduced velocity) where the resonant interaction phenomena between the flow and the wing modes occur. These conclusions underline the importance of designing the initial entrapment of the dynamics into the proper resonance manifolds to achieve efficient and robust suppression.

To numerically prove that the basic underlying dynamic mechanism of instability suppression is a series of resonance captures, we use the empirical mode decomposition introduced in Huang et al. [14]. Although the Morlet wavelet transform gives far better understanding of the temporal evolution of the basic harmonics of a time series compared to the FFT, the WT is essentially an adjustable window Fourier spectral analysis [14] so it may suffer leakage problems due to the finite length of the basic wavelet function. In an alternative numerical postprocessing technique, the EMD through a sifting process yields an empirical basis, a collection of intrinsic mode functions (IMFs) which are complete, almost orthogonal, local, and adaptive. These properties render the EMD applicable to decomposition of nonlinear and nonstationary signals. An IMF is a function that satisfies the following two conditions: 1) the numbers of extrema and of zero crossings must either be equal or must differ at most by 1 in the entire data set considered, and 2) the mean value of the two envelopes defined by the local maxima and local minima must be zero at any time instant. Note that an IMF can be both amplitude- and frequency-modulated; that is, the IMF can be nonstationary. Once EMD is performed, the resulting IMFs are suitable for Hilbert transform, which yields the instantaneous amplitude and phase of each IMF at any given instant of time. By differentiating the instantaneous phase one computes the temporal evolution of the instantaneous frequency of each IMF which, when compared with the overall WT of the time series, enables one to judge the relative contribution of each IMF in the time series and, thus, its relative importance in the decomposition of the signal. Note that an IMF may have a significant contribution in certain time intervals of the signal, and be less important in others. It follows that by decomposing the time series of the NES and wing-mode responses, one may be able to accurately pinpoint the specific IMFs of these

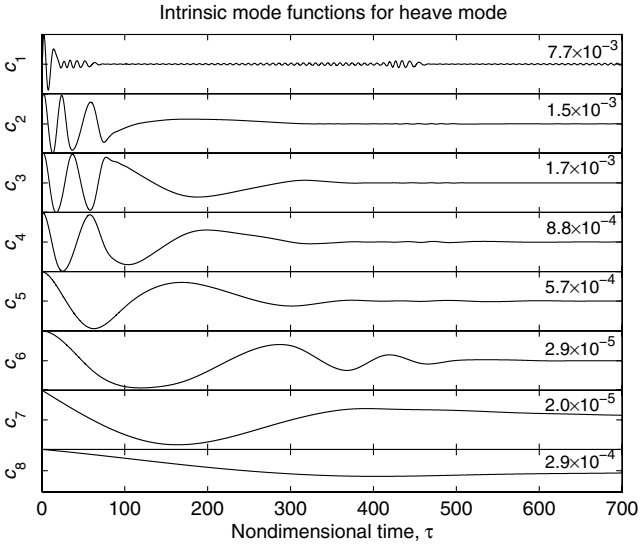

a) Heave

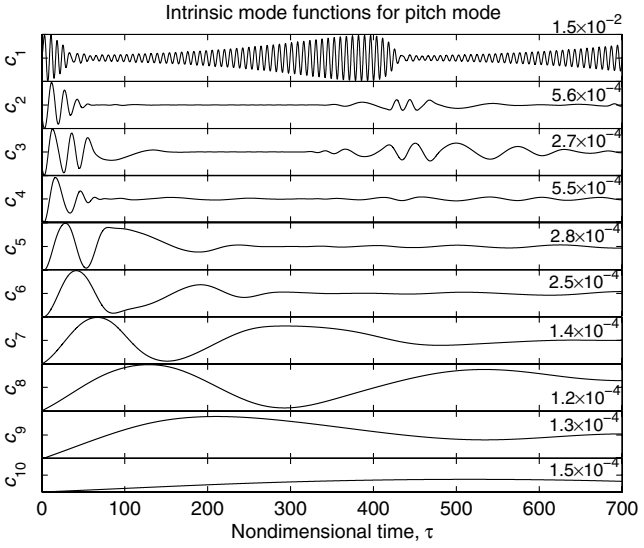

b) Pitch

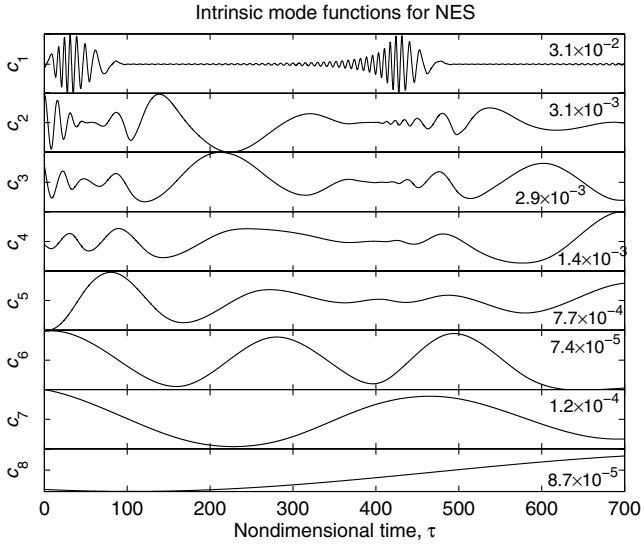

c) NES

Fig. 11 Intrinsic mode functions for the first suppression mechanism in Fig. 3 via empirical mode decomposition. Note that the numbers on the right of each plot indicate the maximum value of the IMF.

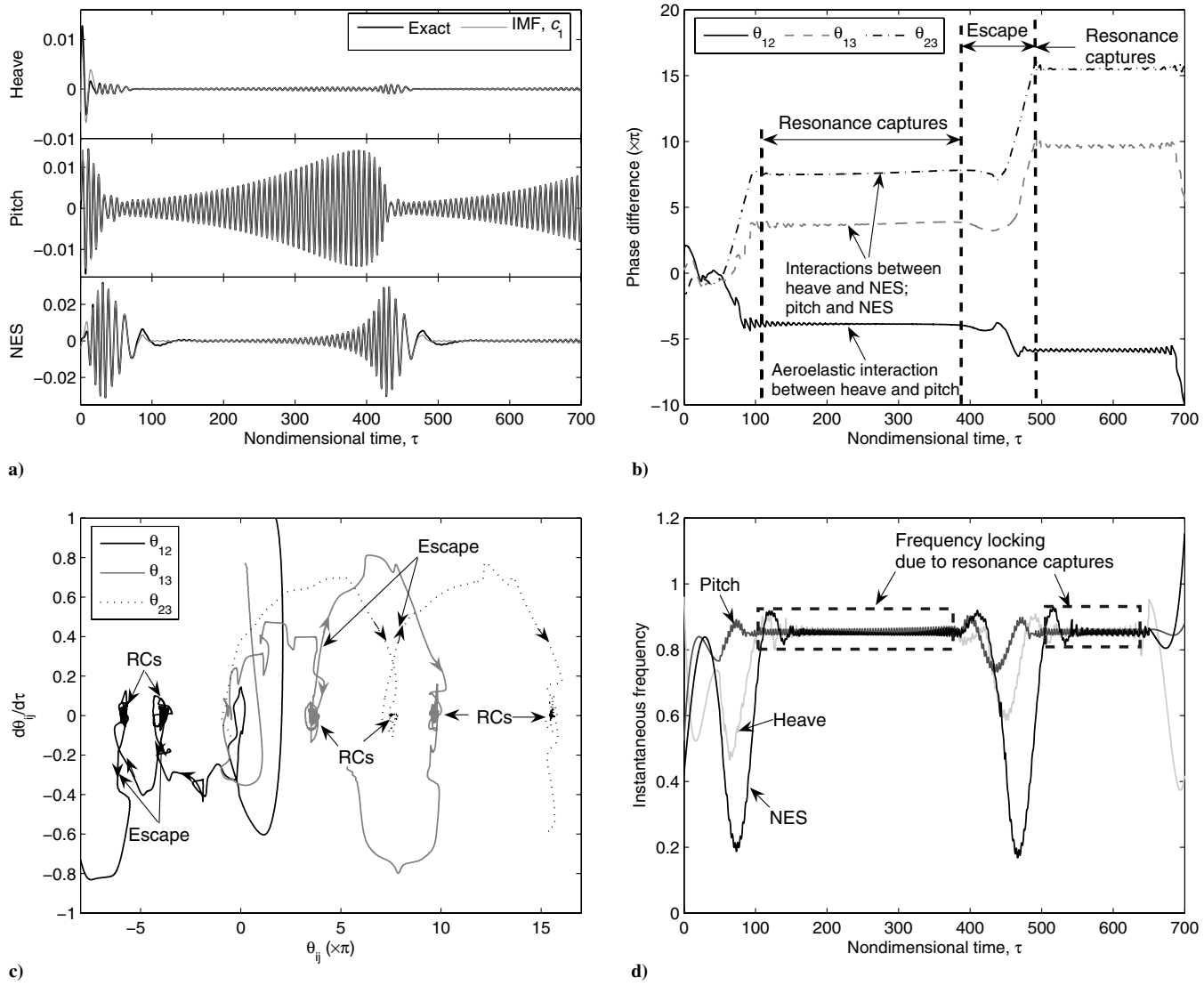

Fig. 12 Numerical investigation of the first suppression mechanism shown in Fig. 3: a) comparison of the leading IMFs with the exact responses, b)–c) phase interactions between the NES and the aeroelastic modes by applying Hilbert transform to the leading IMFs, and d) instantaneous frequencies of each mode.

signals responsible for TET through resonance captures, as well as the specific frequencies where these resonance captures occur. Hence, EMD coupled with the Hilbert transform can be a powerful computational tool for studying complicated nonlinear resonance interactions leading to complex dynamic phenomena (such as TET) in coupled structures. In this study, we use Matlab® codes developed by Rilling et al. [15] to perform the described EMD analysis. The algorithm follows the steps described in the Appendix.

By computing the IMFs, we express the heave, pitch, and NES responses as

$$y(\tau)=\sum_{i=1}^{N_1} c_i(\tau), \qquad \alpha(\tau)=\sum_{i=1}^{N_2} c_i(\tau), \qquad v(\tau)=\sum_{i=1}^{N_3} c_i(\tau) \tag{8}$$

where the ith (complex) IMF $c_i(\tau)$ can be expressed in polar form as $c_i(\tau)=a_i(\tau)e^{j\theta_i(\tau)}$, and the amplitude $a_i(\tau)$ and phase $\theta_i(\tau)$ can be computed from the analytic signal, $z(\tau)=c_i(\tau)+j\mathrm{HT}[c_i(\tau)]$ according to

$$a_i(\tau)=\sqrt{c_i(\tau)^2+\mathrm{HT}[c_i(\tau)]^2}, \qquad \theta_i(\tau)=\tan^{-1}\frac{\mathrm{HT}[c_i(\tau)]}{c_i(\tau)} \tag{9}$$

$\mathrm{HT}[c_i(\tau)]$ is the Hilbert transform of $c_i(\tau)$ computed by

$$\mathrm{HT}[c_i(\tau)]=\frac{1}{\pi}\mathrm{PV}\int_{-\infty}^{\infty}\frac{c_i(s)}{\tau-s}\,\mathrm{d}s \tag{10}$$

where PV indicates the Cauchy principal value of the integral. Therefore, the instantaneous frequency of the ith IMF can be computed as

$$\omega_i(\tau)=\frac{\mathrm{d}\theta_i(\tau)}{\mathrm{d}\tau} \tag{11}$$

We apply the EMD to analyze the NES and wing-mode time series associated with the first suppression mechanism to numerically prove that this mechanism is governed by a series of resonance captures and escapes (transitions) between them. In the next subsection, these results will be compared and verified analytically. All the other suppression mechanisms can be inferred from this consideration so they will not be considered herein. Figure 11 depicts the IMFs of the heave, pitch, and NES modes for the responses shown in Fig. 3. Noting that the number on the upper right part of each plot represents the maximum amplitude of the corresponding IMF, we conclude that the leading (first) IMFs are the dominant oscillatory components of all three responses considered. Figure 12a depicts the comparison of these three leading IMFs, with the

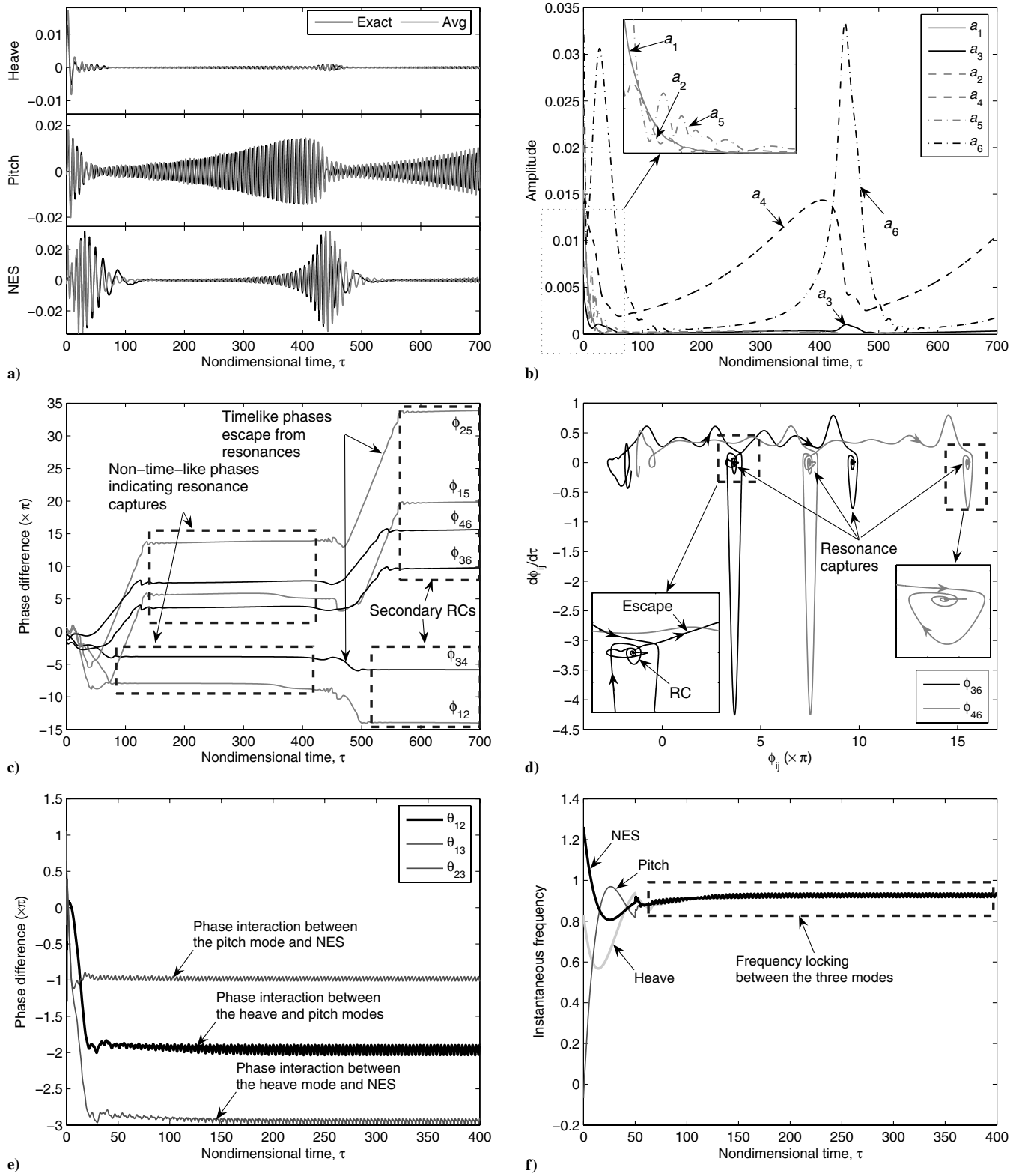

Fig. 13 Analytical suppression mechanism via two-frequency averaging technique. For the first mechanism shown in Fig. 3: a) comparison of the approximate and exact responses, b) instantaneous variation of amplitudes in each frequency component, and c)–d) phase interactions. For the third suppression mechanism shown in Fig. 5: e)–f) phase interactions and instantaneous frequencies (note that the phase variables $\theta_{12,13,23}$ are computed by means of the Hilbert–Huang transforms, i.e., by the Hilbert transform of the leading IMFs).

corresponding time series, from which we observe reasonably good match between them, except for the initial period where the end effect of the EMD appears, and for some lower-frequency intervals where higher-order IMFs may have enhanced contributions in the response.

Let θ_i, $i = 1, 2, 3$ [computed by Eq. (9)] be the phase variables of the three aforementioned leading IMFs of the heave and pitch modes and the NES, respectively. Then, $\theta_{12} \triangleq \theta_1 - \theta_2$ denotes the corresponding phase difference between the heave and pitch modes; $\theta_{13} \triangleq \theta_1 - \theta_3$, the phase difference between the heave mode and the NES; and $\theta_{23} \triangleq \theta_2 - \theta_3$, the phase difference between the pitch mode and the NES.

Figure 12b depicts the temporal evolutions of the instantaneous phase differences θ_{12}, θ_{13}, θ_{23}. If the phase differences show monotonically increasing or decreasing temporal behaviors, they are considered to be *timelike*; otherwise, they are said to exhibit *non-time-like* behavior. For example, a constant or oscillatory phase difference with zero mean over a fixed value is considered to be non-time-like. Clearly, if a phase variable is timelike, it can be considered as a "fast angle" of the dynamics, and, as a result, it may be removed from the dynamics (as nonessential) by simply averaging it out of the problem (in other words, this phase difference will negligibly influence the "slow-flow" dynamics of the system after averaging, and, hence, its contribution is not considered to be important in the time window where the dynamics is analyzed). On the other hand, if the same phase difference is non-time-like, it may not be averaged out of the dynamics (as it cannot be considered to be a fast angle), and it is expected to influence the slow dynamics of the system in the specific time interval of the analysis; in the latter case there occurs resonance capture, and the dynamics is captured transiently into a resonance manifold [16] defined by an integral relation between the instantaneous frequencies of the corresponding IMFs. This resonance capture phenomenon is crucial to understanding TET in this system. This is because, as shown in earlier works [10,17], resonance captures are the dynamic mechanisms for TETs in systems of coupled oscillators. It follows that strong TETs are associated with resonance captures between coupled modes. In Fig. 12, we note that there exist three domains where non-time-like behavior of certain phase differences occurs: 1) $\tau \sim [20, 60]$, 2) $\tau \sim [110, 400]$, and 3) $\tau \sim [490, 700]$. In these time intervals 1:1 resonance captures occur. These RCs appear as spirals in the phase portraits of Fig. 12c. We note that, not only do RCs occur between the heave mode and NES, and between the pitch mode and NES, but, in addition, they also occur between the heave and pitch modes, as in the case of the LCO triggering mechanism [1]. Figure 12d plots the instantaneous frequency of each mode by Eq. (11), and we can clearly see that frequency locking exists whenever RCs occur.

B. Analytical Study

In the preceding section, we found numerically that LCO suppression in the wing under consideration is due to a series of 1:1 or subharmonic resonance captures between the pitch and heave modes and the attached NES. In this section, we also analytically prove this result. Based on the WT results of Fig. 8, we assume the multifrequency decomposition for the heave, pitch, and NES transient responses:

$$y(\tau) = y_1(\tau) + y_2(\tau), \qquad \alpha(\tau) = \alpha_1(\tau) + \alpha_2(\tau)$$
$$v(\tau) = v_1(\tau) + v_2(\tau) \tag{12}$$

where the components with subscripts 1, 2 correspond to slow modulations of the fast frequency components, $e^{j\Omega\tau}$, $e^{j\tau}$, respectively.

In essence, the representations in Eq. (12) are slow–fast multifrequency decompositions of the transient responses, with the fast frequencies determined by the dominant harmonic components identified in the WTs of Fig. 8 (in this case, two fast frequencies). Specifically, the two fast frequencies are the two natural frequencies of the heave and pitch modes in the uncoupled linearized system; we designate these components as LF (lower frequency) and MF (middle frequency) components, respectively, for notational convenience and also for consistency with the notation used in Lee et al. [1].

Introducing the new complex variables [18],

$$\psi_1 = y_1' + j\Omega y_1, \qquad \psi_3 = y_2' + jy_2; \qquad \psi_2 = \alpha_1' + j\Omega\alpha_1$$
$$\psi_4 = \alpha_2' + j\alpha_2; \qquad \psi_5 = v_1' + j\Omega v_1, \qquad \psi_6 = v_2' + jv_2 \tag{13}$$

we express the original variable for the heave mode in the form

$$y = \frac{1}{2j\Omega}(\psi_1 - \psi_1^*) + \frac{1}{2j}(\psi_3 - \psi_3^*)$$
$$y' = \frac{1}{2}(\psi_1 + \psi_1^*) + \frac{1}{2}(\psi_3 + \psi_3^*) \tag{14}$$
$$y'' = \psi_1' + \psi_3' - \frac{j\Omega}{2}(\psi_1 + \psi_1^*) - \frac{j}{2}(\psi_3 + \psi_3^*)$$

Similar expressions hold for the variables corresponding to the pitch mode and the NES.

Substitute the preceding expressions into the equations of motion (2), expressing the complex variables in polar form, $\psi_1(\tau) = \varphi_1(\tau)e^{j\Omega\tau}$, $\psi_3(\tau) = \varphi_3(\tau)e^{j\tau}$; $\psi_2(\tau) = \varphi_2(\tau)e^{j\Omega\tau}$, $\psi_4(\tau) = \varphi_4(\tau)e^{j\tau}$; $\psi_5(\tau) = \varphi_5(\tau)e^{j\Omega\tau}$, $\psi_6(\tau) = \varphi_6(\tau)e^{j\tau}$, where $\varphi_i(\tau)$ is the slowly varying complex-valued amplitude modulation of the respective fast-varying component $e^{j\Omega\tau}$ or $e^{j\tau}$. Applying two-frequency averaging over the two fast components, $e^{j\Omega\tau}$ and $e^{j\tau}$, we obtain a set of six complex-valued modulation equations governing the slow-flow dynamics,

$$\varphi' = \boldsymbol{F}(\varphi) \tag{15}$$

where $\varphi \in \mathbb{C}^6$, and the details of $\boldsymbol{F}$ are not included here (because they are too lengthy to be reproduced in this paper).

Introducing the final polar-form expressions, $\varphi_i(\tau) = a_i(\tau)e^{jb_i(\tau)}$, where $a_i(\tau)$, $b_i(\tau) \in \mathbb{R}$, $i = 1, 2, \ldots, 6$, we express the set of six (complex-valued) slow-flow modulation Eqs. (15) in terms of a set of 12 (real-valued) modulation equations governing the slow evolutions of the amplitudes and phases:

$$\boldsymbol{a}' = \boldsymbol{f}(\boldsymbol{a}, \phi), \qquad \phi' = \boldsymbol{g}(\boldsymbol{a}, \phi) \tag{16}$$

where $\boldsymbol{a} \in \mathbb{R}_+^6$ and $\phi \in S^6$. The slowly varying amplitudes a_1, a_3 (a_2, a_4; a_5, a_6) are, respectively, LF and MF components of the heave (pitch; NES) mode. The independent phase angle vector ϕ possesses the following components:

1) $\phi_{12} = b_1 - b_2$: phase difference between the LF heave and the LF pitch modes

2) $\phi_{34} = b_3 - b_4$: phase difference between the MF heave and the MF pitch modes

3) $\phi_{15} = b_1 - b_5$: phase difference between the LF heave mode and the LF NES

4) $\phi_{25} = b_2 - b_5$: phase difference between the LF pitch mode and the LF NES

5) $\phi_{36} = b_3 - b_6$: phase difference between the MF heave mode and the MF NES

6) $\phi_{46} = b_4 - b_6$: phase difference between the MF pitch mode and the MF NES

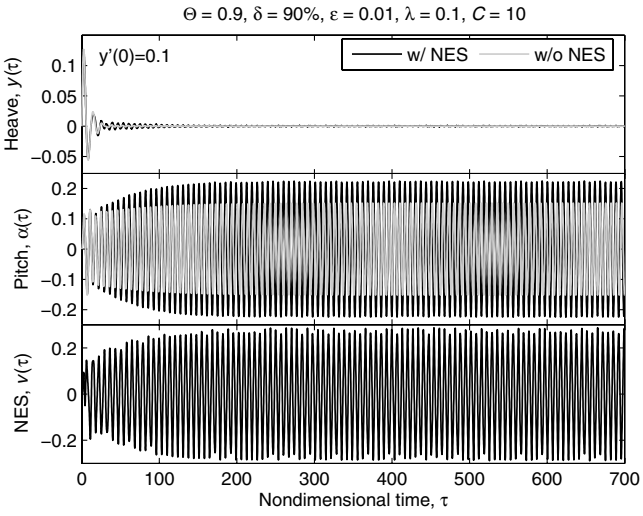

Fig. 14 Breakdown of the first suppression mechanism to form LCOs of larger amplitudes. All the conditions are identical to those used in Fig. 3, except for $y'(0) = 0.1$, which is 10 times larger.

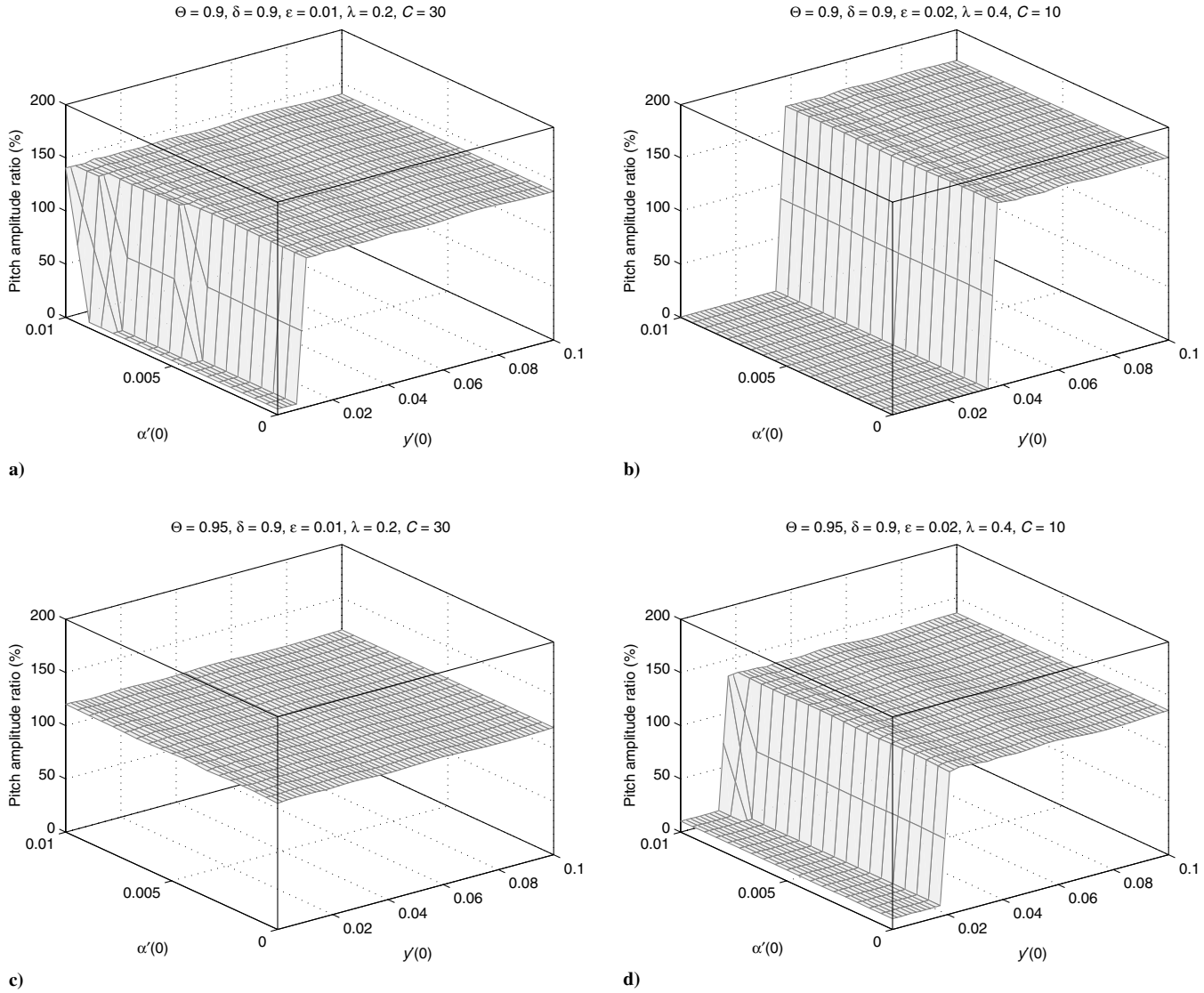

Fig. 15 The steady-state rms pitch amplitude ratio (%), Δ^{α}, with respect to the initial condition set, $\{[y(0), \alpha(0), y'(0), \alpha'(0)]$: $y(0) = \alpha(0) = 0$, $y'(0) \in [0, 0.1]$, and $\alpha'(0) \in [0, 0.01]\}$: $\delta = 0.9$ and a) $\Theta = 0.9$, $\epsilon = 0.01$, $\lambda = 0.2$, $C = 30$; b) $\Theta = 0.9$, $\epsilon = 0.02$, $\lambda = 0.4$, $C = 10$; c) $\Theta = 0.95$, $\epsilon = 0.01$, $\lambda = 0.2$, $C = 30$; d) $\Theta = 0.95$, $\epsilon = 0.02$, $\lambda = 0.4$, $C = 10$.

Note that all independent phase interactions occur between same frequency components (LF–LF or MF–MF).

Figure 13a examines the validity of the averaged system obtained earlier. Except for very low-frequency variations in the NES response, the slow-flow model, Eqs. (12–17), shows good overall match with the original transient dynamics. The discrepancies may be improved if we employ additional fast-frequency components in (12). That is, recalling that the dominant instantaneous frequency in Fig. 12d, is approximately $\omega \approx 0.85$, we conjecture that single-frequency averaging at that fast frequency will be sufficient to capture the important (slow-flow) dynamics of the system; nonetheless, special care must be taken when applying single-frequency averaging as this frequency varies with respect to the flow speed. In fact, some efforts have been made recently to establish sufficiently reasonable slow-flow models by using the HHT, showing that multifrequency averaging is basically equivalent to the HHT [19].

From the evolution of each amplitude component in Fig. 13b, we verify that the MF components are the dominant ones; this result is consistent with the WT results in Fig. 8. Similar resonance captures and escapes are observed as in the numerical study by means of the HHT (Figs. 13c and 13d). An interesting remark is that the resonance captures between the heave and pitch modes occur ahead of those between the heave mode and NES, or those between the pitch mode and NES. This implies that in the first suppression mechanism there occur nonlinear modal energy exchanges between the heave and pitch modes (e.g., the triggering mechanism [1] is activated) before TET to the NES (with the ensuing instability suppression) occurs; this early occurrence of RCs between the heave and pitch modes makes the repetition of suppressions and burstouts in the first suppression mechanism possible. Moreover, it suggests that, for better suppression of LCOs, the NES should interact with the aeroelastic modes before energy transfers between themselves occur (thus preventing the activation of the triggering mechanism for LCO instability). The computations of phase interactions by HHTs in Fig. 13e support this argument, which corresponds to the case of complete elimination of instability (see Fig. 5). Note that the energy transfer from the pitch mode to the NES in this case occurs before the triggering of the pitch from the heave mode, leading to complete elimination of the aeroelastic instability.

IV. Robustness of LCO Suppression

In this section, we investigate the robustness (i.e., dependence on the initial conditions and the change of flow speeds) of the preceding aeroelastic instability suppression mechanisms, by means of steady-state bifurcation analysis of the dynamics of system (2), using numerical continuation of equilibria and periodic solutions. We also explore the effect of offset distance δ on LCO suppression (negative offsets generally appear to give more robust and effective

suppression results). From here on, by positive (negative) attachment, we will mean that the NES is connected to the wing ahead (aft) of the elastic axis; that is, closer to the nose (tail) of the wing. The global bifurcation structure of the dynamics will eventually reveal how the three suppression mechanisms discussed earlier in this paper are related to bifurcations of steady-state solutions. This study will provide hints for NES designs that result in efficient and robust aeroelastic suppression.

The results depicted in Fig. 14 indicate that in some cases, stronger disturbances may eliminate the aforementioned LCO suppressions (that is, LCO suppression may be achieved at certain energy levels but not at others). Indeed, as shown in Fig. 14, increasing the initial velocity by a factor of 10 compared to the value used in Fig. 3 completely eliminates the first suppression mechanism and leads to worse LCOs (e.g., possessing larger amplitudes than the ones realized when no NES is used). Comparing Fig. 14 to Fig. 3, and Fig. 6 to Fig. 5, we see that an issue of robustness of LCO suppression is raised with respect to the effect on the dynamics of changes in initial conditions or flow speed with the other system parameters fixed. Indeed, in both Figs. 14 and 6 the LCOs sometimes reappear with increased amplitudes.

In Fig. 15, the reduction in the steady-state rms pitch amplitude, Δ^{α} by Eq. (3), with respect to the initial condition set, $\{[y(0),\ \alpha(0), y'(0),\ \alpha'(0)]$: $y(0) = \alpha(0) = 0,\ y'(0) \in [0, 0.1]$, and $\alpha'(0) \in [0, 0.01]\}$ is computed. Generally, it appears that the reduction does not depend much on the initial pitching velocity. For a fixed flow speed, increasing the mass ratio and damping broadens the domain of initial conditions where complete elimination or significant reduction of the amplitudes of LCOs occurs. For fixed mass ratio and damping, increasing the flow speed can eliminate or significantly reduce the domain where suppression occurs. It will turn out in the later part of this section that robustness of instability suppression with respect to the initial conditions is highly dependent on the global bifurcation structure.

Robustness of suppression with respect to change of the flow speed also depends on the global dynamical features. Considering the steady-state bifurcation structure, an acceleration of the wing (i.e., increase of rate of changes in the flow speed) will instantly make it possible for the flutter speed to surpass the critical speed when no NES is applied, but the dynamics makes a fast transition to the corresponding steady-state motion. On the other hand, decreasing the flow speed with high deceleration will cause the amplitudes of LCOs to be retained after passing the critical speed until the dynamics reaches its steady state, that is, its trivial equilibrium position.

We use this dependence on the flow speed to investigate steady-state bifurcation behavior by choosing the acceleration or deceleration to be sufficiently small. Figure 16 depicts the computation of peak-to-peak amplitudes when the flow speed increases with the rate $\frac{d\Theta}{d\tau} = 10^{-5}$. For a fixed mass ratio, damping, and nonlinear coupling stiffness, the effects of positive and negative offsets are compared in Figs. 16a and 16b. For a specific reduced speed, a single data point implies a stable trivial equilibrium or a stable LCO; multiple points imply multiperiodic, quasi-periodic, or unstable LCOs. Basically, this methodology is analogous to a frequency-sweeping method when performing modal testing of a structure.

Increasing the flow speed delays the occurrence of the Hopf bifurcation that generates the stable LCOs, when the NES is attached either in positive or negative offsets. Further increasing the speed causes a jump to an LCO of higher amplitude, which implies that there exists a limit point cycle (LPC) bifurcation at the point where the jump occurs; the LPC bifurcation is analogous to the saddle-node bifurcation of equilibrium points. We note that the stable LCO appears to possess quasi periodicity before the jump. Later, we will verify that the quasi periodicity is generated through an NS bifurcation of a periodic solution which is analogous to the Hopf bifurcation of an equilibrium. With a positive NES attachment, the LCOs possess larger amplitudes compared to the case when no NES is attached; on the other hand, smaller LCO amplitudes are obtained with negative attachments. For far higher reduced speeds, the stable

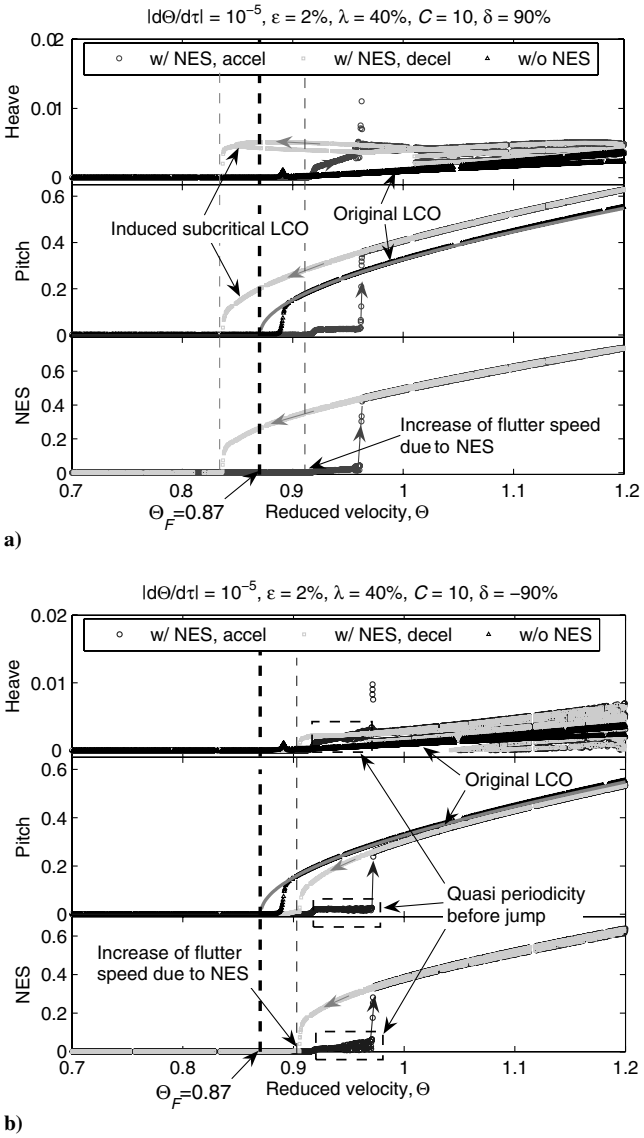

Fig. 16 Bifurcation diagram with respect to the reduced speed Θ by plotting peak–peak amplitudes. Note that only positive amplitudes are depicted: $\frac{d\Theta}{d\tau} = 10^{-5}$, $\epsilon = 0.02$, $\lambda = 0.4$, $C = 10$; a) $\delta = 0.9$ and b) $\delta = -0.9$.

LCOs with larger amplitudes seem to change their periodicity or stability. We will also check that this is true and caused by branch point cycle (BPC) bifurcations. The BPC bifurcation of a periodic solution is similar to a pitchfork or transcritical bifurcation of an equilibrium point [11].

Decreasing the flow speed reveals the clear difference between positive and negative attachments. In both cases there exist branches of unstable periodic solutions connecting the upper and lower branches; in addition, jumps to stable equilibria occur, implying that there exist LPC bifurcations. Whereas the negative attachment produces a jump close to the Hopf bifurcation point, the positive attachment yields a jump at a flow speed even less than the flutter speed for the system with no NES attached. In the latter case the NES clearly leads to further instability, because small disturbances may generate LCOs at flow speeds where only stable trivial equilibria exist in the system with no NES attached.

We further investigate robustness of LCO suppression in terms of the steady-state bifurcation structure, using a numerical continuation method. For this purpose, the *MatCont*, Matlab® code developed by Dhooge et al. [13], was used.

Steady-state bifurcation analysis with respect to (δ, λ) for $\Theta = 0.9$, $C = 10$ is presented in Fig. 17. Smaller ($\epsilon = 0.01$) and larger ($\epsilon = 0.02$) mass ratios are considered; moreover, the contour

plots extracted from Fig. 2 are incorporated into the bifurcation diagram to help the visualization of the steady-state amplitudes. Note that, although our primary interest is to consider offset distances δ in the interval between -1 and 1, in the computational study we extend this interval. By doing that, we can obtain important information on the loci of the Hopf bifurcation points in the (δ, λ) plane.

Figure 17a shows the bifurcation structure for a smaller mass ratio and a fixed flow speed; the corresponding bifurcation diagram for specific damping values is plotted in Fig. 18a. Note that, due to the required computational complexity of the bifurcation study, the stable LCO with larger amplitude (comparable to the LCO of the system with no NES attached) is not displayed in the plot. The Hopf bifurcation curves are located for the offsets at which absolute values are greater than 1, which suggests that we cannot achieve complete elimination within the interval of interest. Moreover, the presence of stable LCOs of large amplitude implies that one cannot obtain robust suppression of LCOs in this case. Clearly, the first and second suppression mechanisms take place within $\delta \in [-1, 1]$; however, a disturbance can eliminate them to give birth to the aforementioned stable LCO. Smaller damping tends to induce more complicated dynamics (the lower plot of Fig. 18a), whereas larger damping eliminates this added complexity.

The steady-state bifurcation structure for the larger mass ratio is presented in Fig. 17b, which depicts global results; the corresponding bifurcation diagrams for typical damping values are provided in Fig. 18b. As in the case of smaller mass ratio, larger damping values tend to eliminate complicated dynamic behaviors. We explain the three LCO suppression mechanisms with the bifurcation analysis for the positive offset attachment. Similar arguments on the suppression mechanisms can be repeated for the negative offsets. First of all, we note that the third suppression mechanism (i.e., complete elimination of LCOs) can be achieved for an offset distance larger than that corresponding to the Hopf bifurcation point. In this case, the suppression is robust, because the bifurcation diagram is global, and there are no other stable equilibria or periodic solutions to "compete" with the stable trivial equilibrium (for example, in the intervals denoted by I_1 and I_2 in the upper part of Fig. 18b). At values below the Hopf bifurcation point (but not below the NS bifurcation point for smaller damping values), we arrive at the second suppression mechanism, which is also robust. By moving the application point toward the e.a. below the NS bifurcation point, the first suppression mechanism appears. Noting that the NS bifurcation implies the generation of another periodic solution, one can draw the conclusion that quasi-periodic behavior is the norm in the first

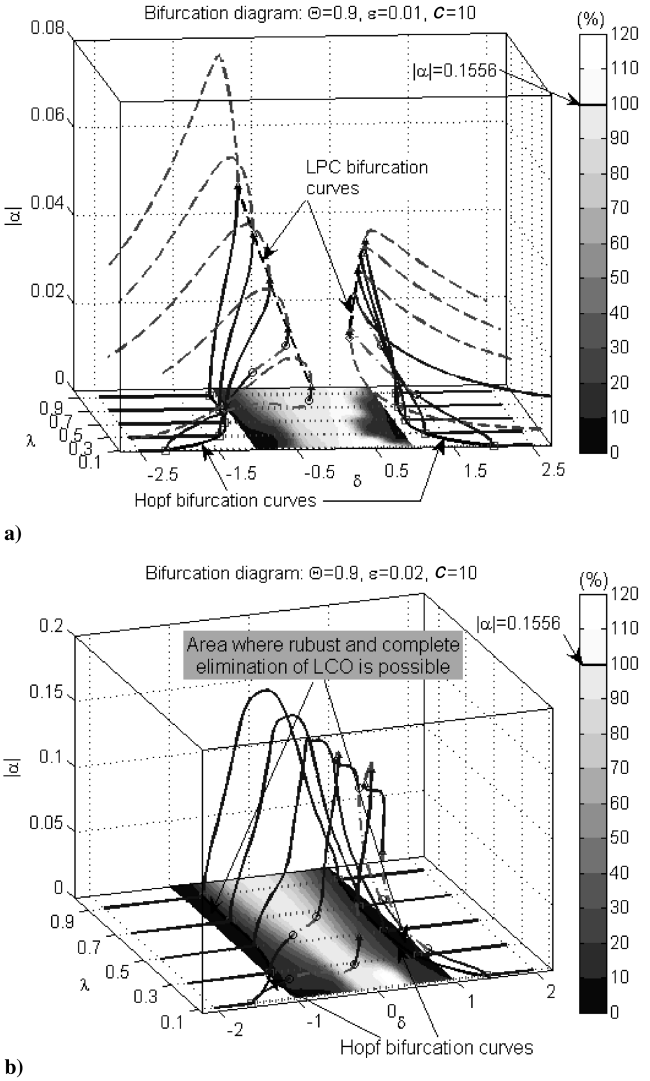

Fig. 17 Steady-state bifurcation behavior with respect to (δ, λ): $\Theta = 0.9$, $C = 10$; a) $\epsilon = 0.01$ and b) $\epsilon = 0.02$. Solid lines indicate stable trivial equilibrium or LCO; dotted lines, unstable trivial equilibrium; dashed lines, unstable LCO; and dash-dotted lines, quasi-periodic LCO. Symbols are used to represent the bifurcation type: square for Hopf, triangle for LPC, circle for NS, and diamond for neutral-saddle (ns) bifurcations.

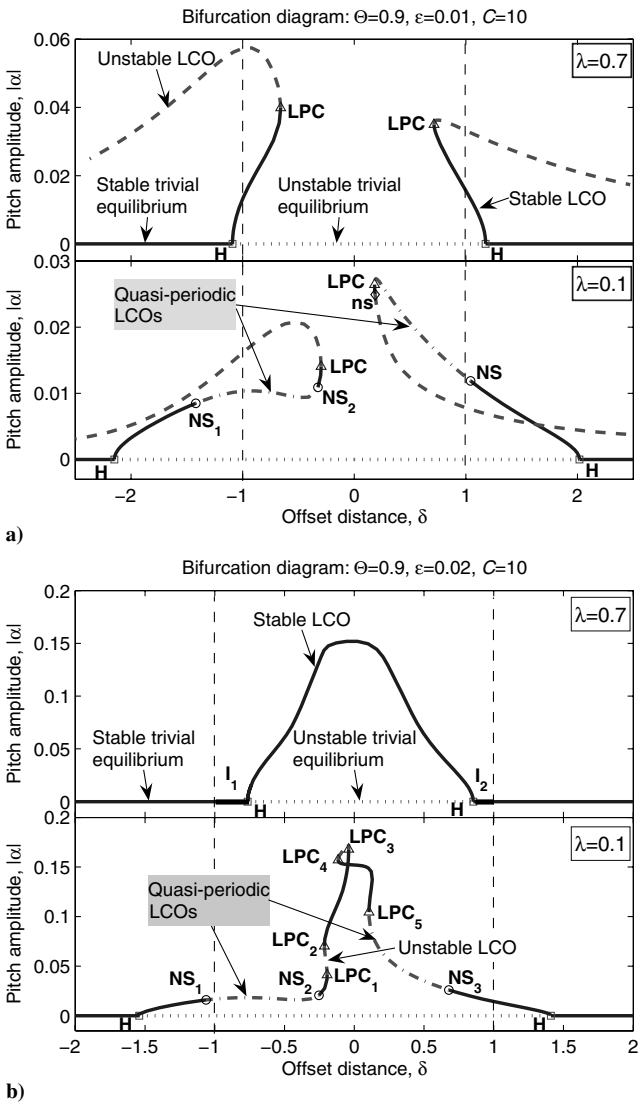

Fig. 18 Bifurcation diagram with respect to the offset δ and fixed damping λ extracted from Fig. 17: $\Theta = 0.9$, $C = 10$; a) $\epsilon = 0.01$ and b) $\epsilon = 0.02$. Note that, because of the computing time, one more stable LCO branch close to the original LCOs without NES is not shown here, which is generated through an LPC bifurcation from the unstable LCO branch extending away from the zero offset.

suppression mechanism (interrupted, however, by instances of periodic motions when the frequency of the new periodic solution is in rational relation to the frequency of the preexisting periodic orbit). Decreasing damping tends to increase the interval where the first suppression mechanism is realized. For sufficiently large values of damping, one cannot observe the occurrence of the first suppression mechanism due to the strong dissipation by the damping forces.

The first suppression mechanism examined in Fig. 3 is recomputed by considering a negative offset distance (Fig. 19). One evident result is that more energy transfer to the NES occurs with $\delta < 0$; whereas the energy transfer to the NES is relatively gradual in Fig. 3, that in Fig. 19a appears to be vigorous. Moreover, a negative attachment extracts more energy from the heave mode, and the duration of the nonlinear resonant interactions between modes lasts longer than the case of positive attachment (i.e., $\tau \sim [380, 500]$ vs $\tau \sim [400, 480]$ for negative and positive attachments, respectively).

In Sec. II, we briefly raised the issue of maximizing the energy dissipation by the NES, which is proportional to $(y' - \delta\alpha' - v')^2$. Examining the responses under condition of 1:1 resonance captures, we can approximate each response roughly such that $y'(\tau) \approx Y \sin\omega\tau$, $\alpha'(\tau) \approx A \sin\omega\tau$, $v(\tau)' \approx V \cos\omega\tau$, where the amplitudes Y, A, V are assumed positive and ω is the frequency value at which frequency locking (resonance capture) occurs. Then, we compute

$$y' - \delta\alpha' - v' \approx (Y - \delta A)\sin\omega\tau - V\cos\omega\tau = X\sin(\omega\tau - \theta) \tag{17}$$

where $X^2 = (Y - \delta A)^2 + V^2$ and $\theta = \tan^{-1}[V/(Y - \delta A)]$.

Clearly, to maximize $(y' - \delta\alpha' - v')^2$, the value of X should be maximum; negative value of δ provides larger values for X, compared to positive δ. Although this may not be a mathematically rigorous description, it helps to get a rough schematic understanding of why negative offsets lead to better and more robust instability suppression compared to positive ones.

Finally, we wish to relate the effects of offset distance to the bifurcation analysis with respect to the reduced speed. Figures 20a and 20b show the steady-state bifurcation behavior with respect to offset distance and reduced velocity. Because the qualitative aspects are similar to each other, we focus only on the case of positive attachment. For zero offset distance, the bifurcation behavior is equivalent to the case when no NES is applied. By increasing the offset distance away from the e.a., the occurrence of the Hopf bifurcation is delayed with respect to an increase of the flow speed; moreover, the intervals where quasi-periodic responses occur (i.e., the first suppression mechanism) widen, as are the intervals between the two LPC bifurcation points. In this case, the BPC bifurcation point converges to the smaller LPC bifurcation point, and the Hopf bifurcation curves are almost symmetric with respect to $\delta = 0$.

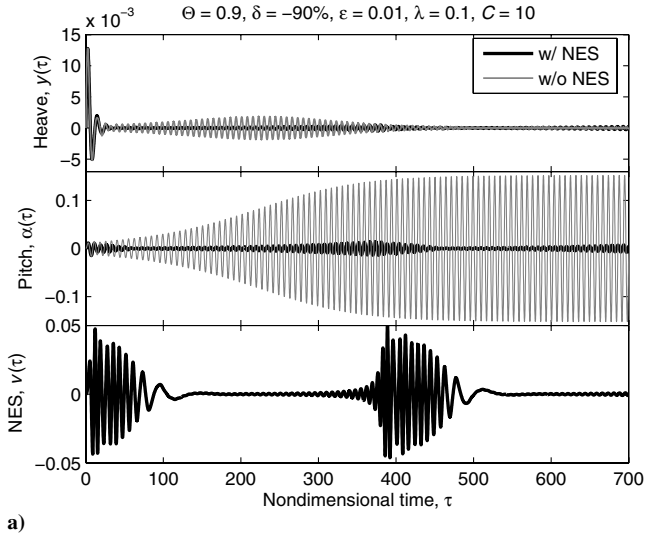

a)

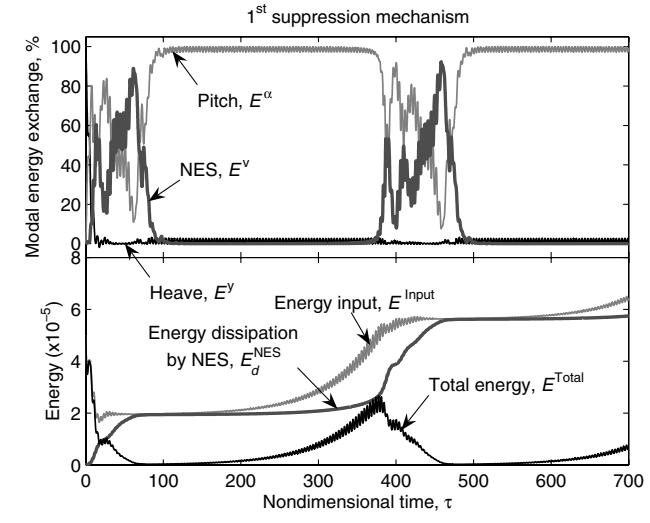

b)

Fig. 19 The first suppression mechanism using the same conditions as in Fig. 3 except the offset distance, $\delta = -0.9$: a) time responses, b) instantaneous energy exchanges between modes.

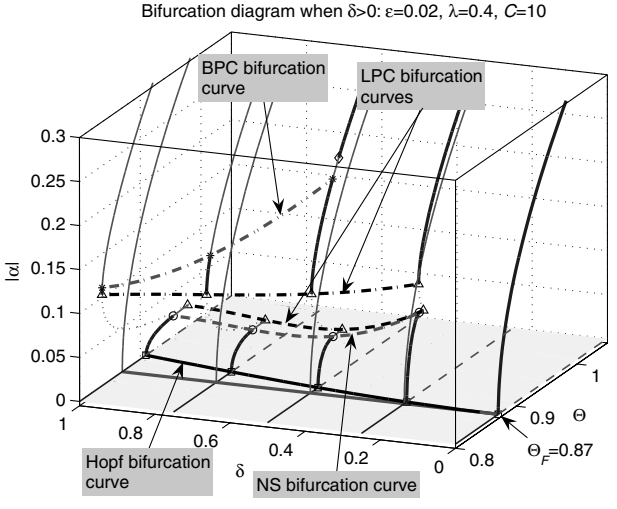

a)

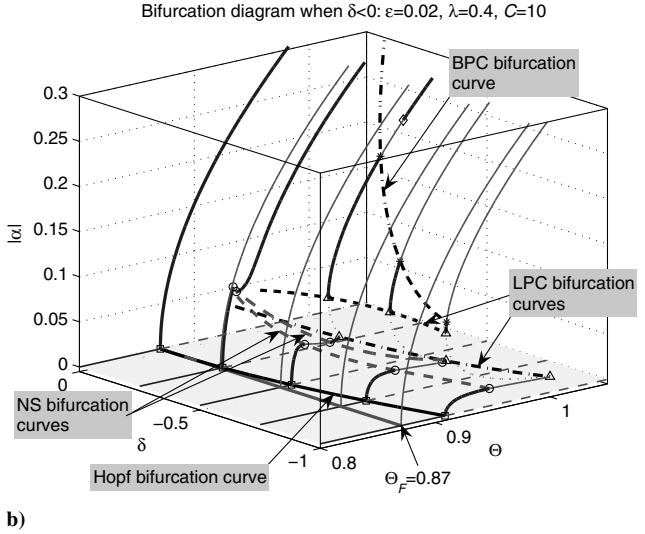

b)

Fig. 20 Steady-state bifurcation behavior with respect to Θ: $\epsilon = 0.02$, $\lambda = 0.4$, $C = 10$; a) positive offset ($\delta > 0$) and b) negative offset ($\delta < 0$). Similar notations are used as in Fig. 17 and the asterisk stands for a BPC bifurcation.

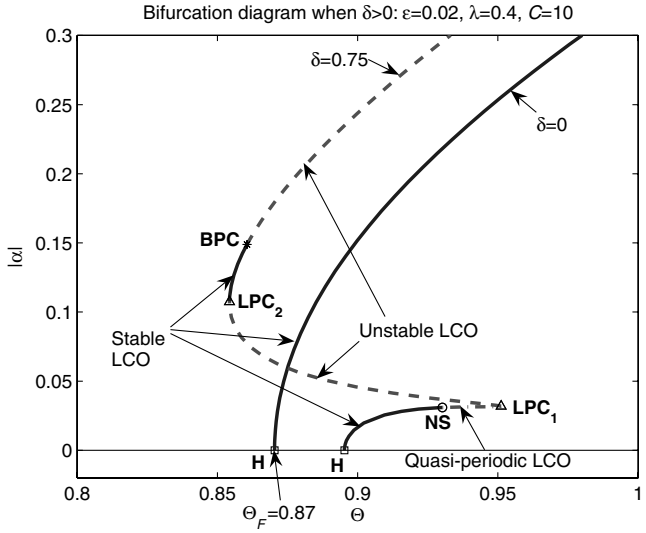

a)

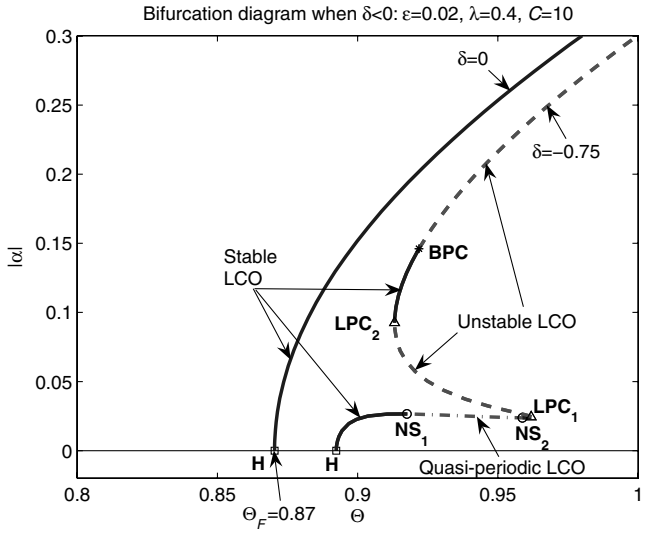

b)

Fig. 21 Typical bifurcation diagram extracted from Fig. 20: a) positive offset ($\delta = 0.75$) and b) negative offset ($\delta = -0.75$).

Typical bifurcation diagrams shown in Fig. 21 reaffirm the quantitative differences between the positive and negative attachments, which were explained in Fig. 16. Positive attachments generally lead to LCOs of larger amplitude compared to those of the system with no NES attached, whereas negative attachments yield smaller amplitude LCOs. In terms of the suppression mechanisms, we observe the sequence from the third to the first mechanisms by increasing the flow speed. Further increase of the flow speed above the LPC_1 bifurcation point will produce a sudden jump to LCOs of larger amplitudes. A wing-NES system with a bifurcation structure similar to that depicted in Fig. 21b is a configuration suitable for practical applications.

V. Conclusions

We investigated the suppression of aeroelastic instabilities in a 2-DOF wing system by means of passive, broadband, nonlinear targeted energy transfers. The physical mechanism for inducing these transfers was a lightweight, essentially nonlinear oscillator attachment termed nonlinear energy sink. Through numerical parametric studies we found that there exist three suppression mechanisms for suppressing aeroelastic instabilities in this system. We investigated these mechanisms numerically and analytically, and proved that the underlying dynamic mechanisms governing them were series of resonance captures, for example, of transient resonances either between the NES and the heave and/or pitch modes, or between the wing modes themselves. We explored these mechanisms in terms of steady-state bifurcation analysis, which addressed the issue of the robustness of the suppression, that is, of dependence on initial conditions and the parameters of the problem. We found that NESs attached with negative offsets can provide robust aeroelastic instability suppression within wide ranges of system parameters; on the contrary, NESs with positive offsets do not provide robust suppression, as explained by the associated series of bifurcations that occur for positive offsets. It follows that lightweight NESs with negative offsets can form the basis of practical, economical, robust and realistic designs for LCO suppression in the wing under consideration. These theoretical observations are verified experimentally in a companion paper [8].

Appendix: Algorithm for Empirical Mode Decomposition

We summarize the algorithm of computing the intrinsic mode functions of a signal $x(t)$, which is introduced in Rilling et al. [15]. For more technical details on the empirical mode decomposition, refer to Huang et al. [14].

The main loop for extracting IMFs is as follows:

1) Identify all extrema of $x(t)$.

2) Perform interpolations between minima [maxima], ending up with some envelope $e_{\min}(t)$ [$e_{\max}(t)$].

3) Compute the average $R(t) = [e_{\min}(t) + e_{\max}(t)]/2$ (as a residual).

4) Extract the detail $c(t) = x(t) - R(t)$.

5) Iterate on the residual $R(t)$.

In practice, the preceding procedure is refined by a *sifting* process, and the inner loop that iterates 1–4 on the detail $c(t)$ runs until the average $R(t)$ can be considered as zero mean under some tolerance (i. e., as a stopping criterion). Once it is achieved, the detail $c(t)$ is regarded as the effective IMF. By repetition, the original signal $x(t)$ then can be decomposed as

$$x(t) = \sum_{k=1}^{N} c_k(t) + R^{N+1}(t)$$

Figure 22 depicts schematic extraction of IMFs from a signal $x(t) = \sin 2\pi t + \sin 6\pi t$. Because there are no controls of the sifting process, end effects appear. Following the notation used in Sec. III, the IMFs are computed as $c_1(t) \approx \sin 6\pi t$ (i.e., the high-frequency component is extracted first), and $c_2(t) = x(t) - c_1(t) \approx \sin 2\pi t$.

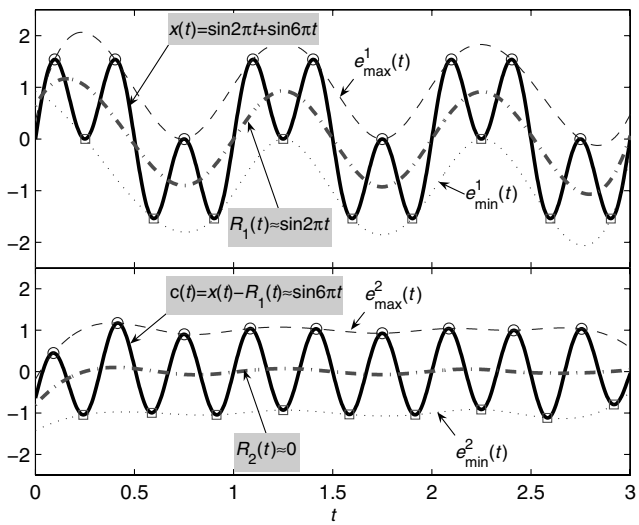

Fig. 22 Schematic of the empirical mode decomposition of $x(t) = \sin \omega_0 t + \sin 3\omega_0 t$ where $\omega_0 = 2\pi$.

Acknowledgments

This work was supported by the U.S. Air Force Office of Scientific Research through Grant Number FA9550-04-1-0073. GK would like to acknowledge support from the Belgian National Fund for Scientific Research (FNRS), which made his visit to the University of Illinois possible.

References

[1] Lee, Y., Vakakis, A., Bergman, L., McFarland, D., and Kerschen, G., "Triggering Mechanisms of Limit Cycle Oscillations in a Two-Degree-of-Freedom Wing Flutter Model," *Journal of Fluids and Structures*, Vol. 21, Nos. 5–7, 2005, pp. 485–529.

[2] Dowell, E., "Non-Linear Oscillator Models in Bluff Body Aeroelasticity," *Journal of Sound and Vibration*, Vol. 75, No. 2, 1981, pp. 251–264.

[3] Ko, J., Kurdila, A., and Strganac, T., "Nonlinear Control of a Prototypical Wing Section with Torsional Nonlinearity," *Journal of Guidance, Control, and Dynamics*, Vol. 20, No. 6, 1997, pp. 1181–1189.

[4] Friedmann, P., Guillot, D., and Presente, E., "Adaptive Control of Aeroelastic Instabilities in Transonic Flow and Its Scaling," *Journal of Guidance, Control, and Dynamics*, Vol. 20, No. 6, 1997, pp. 1190–1199.

[5] Fatimah, S., and Verhulst, F., "Suppressing Flow-Induced Vibrations by Parametric Excitation," *Nonlinear Dynamics*, Vol. 31, No. 3, 2003, pp. 275–297.

[6] Tondl, A., Ruijgrok, M., Verhulst, F., and Nabergoj, R., *Autoparametric Resonance in Mechanical Systems*, Cambridge Univ. Press, New York, 2000.

[7] Lee, Y., Vakakis, A., Bergman, L., and McFarland, D., "Suppression of Limit Cycle Oscillations in the van der Pol Oscillator by Means of Passive Nonlinear Energy Sinks (NESs)," *Structural Control and Health Monitoring*, Vol. 13, No. 1, 2006, pp. 41–75.

[8] Lee, Y., Kerschen, G., McFarland, D., Hill, W., Nichkawde, C., Strganac, T., Bergman, L., and Vakakis, A., "Suppressing Aeroelastic Instability Using Broadband Passive Targeted Energy Transfers, Part 2: Experiments," *AIAA Journal* (submitted for publication).

[9] Dowell, E., Crawley, E., Jr., Curtiss, H. C., Jr., Peters, D., Scanlan, R., and Sisto, F., *A Modern Course in Aeroelasticity*, Kluwer Academic Publishers, Dordrecht, The Netherlands, 1995.

[10] Kerschen, G., Lee, Y., Vakakis, A., McFarland, D., and Bergman, L., "Irreversible Passive Energy Transfer in Coupled Oscillators with Essential Nonlinearity," *SIAM Journal on Applied Mathematics*, Vol. 66, No. 2, 2006, pp. 648–679.

[11] Kuznetsov, Y., *Elements of Applied Bifurcation Theory*, Springer–Verlag, New York, 1995.

[12] Lee, Y., Kerschen, G., Vakakis, A., Panagopoulos, P., Bergman, L., and McFarland, D., "Complicated Dynamics of a Linear Oscillator with a Light, Essentially Nonlinear Attachment," *Physica D*, Vol. 204, Nos. 1–2, 2005, pp. 41–69.

[13] Dhooge, A., Govaerts, W., and Kuznetsov, Y., "MATCONT: A Matlab Package for Numerical Bifurcation Analysis of ODEs," *ACM Transactions on Mathematical Software*, Vol. 29, No. 2, 2003, pp. 141–164.

[14] Huang, N., Shen, Z., Long, S., Wu, M., Shih, H., Zheng, Q., Yen, N.-C., Tung, C., and Liu, H., "The Empirical Mode Decomposition and the Hilbert Spectrum for Nonlinear and Non-Stationary Time Series Analysis," *Proceedings of the Royal Society of London. Series A*, Vol. 454, No. 1971, 1998, pp. 903–995.

[15] Rilling, G., Flandrin, P., and Gonçalvès, P., "On Empirical Mode Decomposition and Its Algorithms," *IEEE-Eurasip Workshop on Nonlinear Signal and Image Processing (NSIP-03)*, Grado, Italy, June 2003.

[16] Arnold, V., *Dynamical Systems 3, Encyclopaedia of Mathematical Sciences*, Springer–Verlag, Berlin, 1988.

[17] Vakakis, A., and Gendelman, O., "Energy Pumping in Coupled Mechanical Oscillators, Part 2: Resonance Capture," *Journal of Applied Mechanics*, Vol. 68, Jan. 2001, pp. 42–48.

[18] Manevitch, L., "The Description of Localized Normal Modes in a Chain of Nonlinear Coupled Oscillators Using Complex Variables," *Nonlinear Dynamics*, Vol. 25, Nos. 1–3, 2001, pp. 95–109.

[19] Kerschen, G., Vakakis, A., Lee, Y., McFarland, D., and Bergman, L., "Toward a Fundamental Understanding of the Hilbert-Huang Transform," *The International Modal Analysis Conference (IMAC) 24: A Conference and Exposition on Structural Dynamics*, Paper 31, Society for Experimental Mechanics, Bethel, CT, Jan.–Feb. 2006.

M. Ahmadian
Associate Editor